BMC Medicine

RESEARCH

Open Access

Hyperactivation of ATF4/TGF-β1 signaling contributes to the progressive cardiac fibrosis in Arrhythmogenic cardiomyopathy caused by *DSG2* Variant

Baowei Zhang[1†], Yizhang Wu[1†], Chunjiang Zhou[1], Jiaxi Xie[2], Youming Zhang[1], Xingbo Yang[3], Jing Xiao[3], Dao Wu Wang[4], Congjia Shan[5], Xiujuan Zhou[2], Yaozu Xiang[3*] and Bing Yang[1*]

Abstract

Background Arrhythmogenic cardiomyopathy (ACM) is an inherited cardiomyopathy characterized with progressive cardiac fibrosis and heart failure. However, the exact mechanism driving the progression of cardiac fibrosis and heart failure in ACM remains elusive. This study aims to investigate the underlying mechanisms of progressive cardiac fibrosis in ACM caused by newly identified *Desmoglein-2 (DSG2)* variation.

Methods We identified homozygous $DSG2^{F531C}$ variant in a family with 8 ACM patients using whole-exome sequencing and generated $Dsg2^{F536C}$ knock-in mice. Neonatal and adult mouse ventricular myocytes isolated from $Dsg2^{F536C}$ knock-in mice were used. We performed functional, transcriptomic and mass spectrometry analyses to evaluate the mechanisms of ACM caused by $DSG2^{F531C}$ variant.

Results All eight patients with ACM were homozygous for $DSG2^{F531C}$ variant. $Dsg2^{F536C/F536C}$ mice displayed cardiac enlargement, dysfunction, and progressive cardiac fibrosis in both ventricles. Mechanistic investigations revealed that the variant DSG2-F536C protein underwent misfolding, leading to its recognition by BiP within the endoplasmic reticulum, which triggered endoplasmic reticulum stress, activated the PERK-ATF4 signaling pathway and increased ATF4 levels in cardiomyocytes. Increased ATF4 facilitated the expression of TGF-β1 in cardiomyocytes, thereby activating cardiac fibroblasts through paracrine signaling and ultimately promoting cardiac fibrosis in $Dsg2^{F536C/F536C}$ mice. Notably, inhibition of the PERK-ATF4 signaling attenuated progressive cardiac fibrosis and cardiac systolic dysfunction in $Dsg2^{F536C/F536C}$ mice.

Conclusions Hyperactivation of the ATF4/TGF-β1 signaling in cardiomyocytes emerges as a novel mechanism underlying progressive cardiac fibrosis in ACM. Targeting the ATF4/TGF-β1 signaling may be a novel therapeutic target for managing ACM.

Keywords Arrhythmogenic cardiomyopathy, Desmoglein 2, Cardiac fibrosis, Transforming growth factor β1, Activating transcription factor 4

[†]Baowei Zhang and Yizhang Wu contributed equally as first authors.

*Correspondence:
Yaozu Xiang
yaozu.xiang@tongji.edu.cn
Bing Yang
bingyang@tongji.edu.cn
Full list of author information is available at the end of the article

Background

Arrhythmogenic cardiomyopathy (ACM) is an inherited cardiomyopathy characterized by ventricular arrhythmias, high risks of sudden death and progressive heart failure [1]. Implantable cardioverter defibrillators and radiofrequency ablation have significantly reduced the risk of ventricular arrhythmias and sudden death, however, patients with ACM are still threatened by progressive heart failure. The pathological features of ACM are marked by cardiomyocyte loss and cardiac fibrosis [2], which may contribute to the progressive heart failure. Genetic variations in genes encoding desmosomal proteins account for approximately two-thirds of ACM cases [3]. Desmoglein 2 (DSG2), a transmembrane protein encoded by *DSG2*, is an important component of desmosome complex [4]. Since its discovery as a causative gene for ACM in 2006 [5], *DSG2* has consistently ranked as the second most prevalent pathogenic gene associated with ACM [6]. Additionally, ACM patients with pathogenic *DSG2* variations have high likelihood of left ventricular fibrosis and cardiac systolic dysfunction [7]. While previous studies have highlighted the involvement of disrupted desmosomal adhesion, Wnt signaling, and inflammation in ACM [8–13], the mechanism underlying the progressive cardiac fibrosis in ACM caused by pathogenic *DSG2* variations remains unclear. Furthermore, there is currently a lack of effective treatments to mitigate or reverse the progressive cardiac dysfunction in ACM.

The endoplasmic reticulum (ER), the primary site for the folding and post-translational modification of membrane proteins, plays a crucial role in maintaining protein homeostasis in eukaryotic cells [14]. However, under conditions of inflammation, hypoxia, or gene variation, accumulated misfolded or unfolded proteins in the ER could induce ER stress and activate the unfolded protein response (UPR), promoting apoptosis, inflammation, fibrosis, and other detrimental effects in various diseases [15]. However, the role of UPR in ACM caused by variant *DSG2* is unclear.

Previous studies, including our own, have identified the *DSG2* missense variant c.1592 T > G (rs200484060) in patients with ACM [16–19]. This variant leads to the substitution of phenylalanine with cysteine at codon site 531 (p. F531C), which is located in the extracellular anchoring domain of DSG2. In silico analysis indicated a high likelihood of this missense variant having a detrimental impact on the structure and function of the protein (Polyphen: probably damaging; SIFT: deleterious). Nevertheless, the pathogenicity and underlying mechanisms of this variant in ACM are still not fully understood. Given that DSG2 is a transmembrane protein, we postulated that the UPR may be activated and involved in the progressive cardiac fibrosis in ACM caused by the $DSG2^{F531C}$ variant.

In the present study, we conducted genetic sequencing of a five-generation family affected by ACM. All eight patients diagnosed with ACM were homozygous for $DSG2^{F531C}$ variant. Subsequently, we developed a knock-in mouse model carrying the mouse-equivalent form ($Dsg2^{F536C}$) of this variant. Homozygous knock-in mice exhibited overt cardiac phenotypes highly similar to the clinical manifestations of ACM. Through mechanistic investigations, we demonstrated that the variant DSG2 (vDSG2) in cardiomyocytes was misfolded and triggered protein kinase R like ER kinase (PERK)—activating transcription factor 4 (ATF4) signaling, leading to an increase in the expression of transforming growth factor β1 (TGF-β1). This activated cardiac fibroblasts via paracrine signaling, ultimately promoting cardiac fibrosis in $Dsg2^{F536C/F536C}$ mice. Inhibition of the PERK-ATF4 signaling attenuated the elevated TGF-β1 levels, ameliorated the progressive cardiac fibrosis and dysfunction in $Dsg2^{F536C/F536C}$ mice. These findings highlight the hyperactivation of the ATF4/TGF-β1 signaling in cardiomyocytes as a novel mechanism driving progressive cardiac fibrosis in ACM, suggesting that targeting the ATF4/TGF-β1 signaling could serve as a potential therapeutic strategy for ACM.

Methods

Human study

This study involved 48 individuals from a large family in China. The proband was diagnosed with ACM during hospitalization for ventricular tachycardia at the First Affiliated Hospital of Nanjing Medical University. All family members were clinically evaluated according to the guideline for management of ACM, which included clinical history, 12-lead electrocardiography (ECG) and transthoracic echocardiography [20, 21]. In addition, 24-h ambulatory ECG and cardiac magnetic resonance imaging (MRI) were performed on some participants. This study was approved by the Ethics Committee of the First Affiliated Hospital of Nanjing Medical University (NO.2011-SR-014) and informed consent was obtained from all participants prior to evaluation and testing.

Genomic DNA from all family members was extracted from peripheral blood samples using QIAamp DNA Blood Mini Kits (Qiagen). Sanger sequencing was performed to analyze the five desmosome-encoding genes (*DSG2, DSC2, JUP, PKP2, DSP*) as well as the *TMEM43* and *PLN* genes, as previously reported [16]. To further explore whether additional genes beyond those mentioned above were associated with ACM, whole-exome sequencing was performed in the proband using the

Agilent SureSelect Human All Exon V6 Kit on the Hiseq X Ten. The ACMG criteria were applied to evaluate the pathogenicity of identified variants. Novel nonsynonymous variants were assessed in a population of 950 ethnically matched healthy controls.

Animal experiments

Animal experiments were approved by the Institutional Animal Care and Use Committee of Nanjing Medical University (approval number: IACUC-14030160). All animal procedures were performed in accordance with the National Institutes of Health Guide for the Care and Use of Laboratory Animals. General anesthesia was induced using a 1%-3% inhaled isoflurane/oxygen mixture. The mice were housed under specific pathogen-free conditions with 12-h dark–light cycles and had free access to food and water. Animals of both sexes were used in the experiments without bias. All mice were euthanized by cervical dislocation after deep anesthesia using a 5% isoflurane/oxygen mixture.

Dsg2^{F536C} mice were generated using homologous recombination technology as previously described [22, 23]. Briefly, the targeting construct, which included the F536C point variant and a neomycin cassette flanked by Loxp sites, was designed and electroporated into embryonic stem cells (ESCs) (Additional file 1: Fig. S3a). After genotyping by Southern blotting, the targeted ESCs were injected into C57BL/6 J blastocysts to generate mouse chimeras (Additional file 1: Fig. S3b). By crossing the chimeras with CMV-Cre mice, the neomycin cassette was removed, and the heterozygous *Dsg2*$^{F536C/WT}$ progeny were generated after backcrossing with C57BL/6 J mice. This backcrossing process was repeated for at least 4 generations to eliminate background diversity. Subsequently, heterozygous intercrosses of *Dsg2*$^{F536C/WT}$ mice were used to obtain cohorts of homozygous *Dsg2*$^{F536C/F536C}$, heterozygous *Dsg2*$^{F536C/WT}$ and wild-type *Dsg2*$^{WT/WT}$ mice for this variant. Further sequencing analysis for the polymerase chain reaction (PCR) product confirmed the positive mutation leading to the substitution of phenylalanine with cysteine (Additional file 1: Fig. S3c). Subsequently, PCR strategy was carried out to identify the wild-type allele (368 bp) and the mutant allele (466 bp) (Additional file 1: Fig. S3d).

Echocardiography was performed under inhaled anesthesia with 1% to 3% isoflurane/oxygen mixture. The mice were maintained at an appropriate state, with heart rate at about 450 bpm and temperature at about 37 °C. Images were obtained using a mouse transthoracic echocardiography system equipped with a 30-MHz linear transducer (Vevo2100; VisualSonics Inc) at a sweep speed of 200 mm/s. The left ventricular geometry and systolic function were assessed in the short-axis view at the level of the papillary muscles. All the procedures were performed by the same researcher, who was blinded to the genotype.

Electrocardiographic measurements were performed under the same anesthesia conditions as the echocardiography. Limb-lead surface ECGs were recorded using subcutaneous 23-gauge needle electrodes attached to each limb. The ECGs were continuously recorded by the Powerlab acquisition system (AD Instruments) and analyzed with IOX Software (EMKA) and Chart5 Pro analysis software (AD Instruments). To accurately measure the duration and amplitude of the P wave and QRS complex, we selected ECG segments with a stable baseline and excluded any instances of arrhythmias. The P wave was marked from the beginning of the P wave to the point where it returned to the iso-electrical line. The QRS complex was measured from the onset of the first deflection of the QRS complex to the point where the last returned to the baseline [24]. The measurement and analysis of ECG parameters were performed by the same professional cardiac electrophysiologist, who was blinded to the genotype. After ECG recording, the mice were euthanized and their hearts were excised for further study, either by freezing at -80 °C or by fixing in 4% paraformaldehyde (PFA)/OCT Compound (Sakura).

Histological analysis

Frozen Sects. (5 μm) were used for immunofluorescence staining. The sections were fixed with 4% PFA for 1 h and then washed with PBS. Antigen retrieval was performed by boiling in sodium citrate for 2 min, followed by permeabilization with 1% Triton X-100 (Sigma-Aldrich) for 15 min. After washing with PBS, the sections were blocked with 1% bovine serum albumin (BSA) for 45 min and incubated with primary antibodies at 4℃ overnight. The sections were then washed in PBS and incubated with the secondary antibodies for 1 h at room temperature. Following additional PBS washes, the sections were stained with DAPI (Invitrogen) and mounted with Prolong Gold Antifade Mountant (Invitrogen). The slides were scanned with laser scanning confocal microscopy (Nikon) and analyzed with Image Pro Plus 6.0.

To assess the extent of fibrosis throughout the ventricles, the paraffin-embedded hearts were serially sectioned from the apex to the base into 10 μm slices. At least five mice of the same age and genetic background were included in each group to assess cardiac fibrosis and ventricular wall thickness ($n \geq 5$ in each group). For each heart, eight levels of paraffin sections from the apex to the base were selected for Masson's trichrome staining (Nanjing Jiancheng Bioengineering Institute), and observed under a light microscope. The collagen volume fraction (CVF) and ventricular wall thickness were

measured using Image Pro Plus 6.0. The CVF was calculated as the ratio of the collagen area to the total tissue area in each slice. The CVF of the entire heart was determined by averaging the CVF values from the 8 selected tissue sections. The measurement method for ventricular wall thickness is the same as in our previous publication [25]. Briefly, the thickness of the left ventricular free wall, the interventricular septum, and the right ventricular free wall were measured at the level of the left ventricular papillary muscles. The minimal value among these measurements was selected as the final ventricular wall thickness.

Paraffin Sects. (5 μm) were prepared and stained for immunohistochemistry according to standard procedures. After baking at 60 °C for 30 min, the sections were deparaffinized, underwent antigen retrieval, and were subjected to endogenous peroxidase and protein blocking. Primary and secondary antibody incubations were performed sequentially, followed by DAB staining and hematoxylin counterstaining. Isotype control antibody staining was performed simultaneously. The slides were then scanned with light microscopy and analyzed using Image Pro Plus 6.0.

Plasmid construction and transfection

HEK293T cells were purchased from ATCC and cultured in Dulbecco's modified Eagle's medium (DMEM) supplemented with 10% fetal bovine serum (FBS) and 1% penicillin/streptomycin. The pcDNA3.1 vector containing cDNA of mouse *Dsg2* and a C-terminal 3xFlag epitope was purchased from Youbio Bio lnc. PCR with high-fidelity DNA polymerase (Q5 High-Fidelity 2X Master Mix, NEB) was performed to construct the plasmid with a *Dsg2* site mutation. After confirming the *Dsg2* variant by DNA sequencing, pcDNA3.1 vectors with wild-type *Dsg2* and variant *Dsg2* were used to transfect HEK293T cells (Lipo 8000 transfection reagent, Beyotime Bio.) to overexpress the wild-type DSG2 (wtDSG2) and vDSG2.

HL-1 cells culture and lentiviral transfection

HL-1 cells were cultured in dishes coated with gelatin/fibronectin and maintained in Claycomb culture medium supplemented with 10% FBS, 0.1 mM norepinephrine, 2 mM L-glutamine and 1% penicillin/streptomycin. Wild-type and variant mouse *Dsg2* cDNA with AscI and PacI restriction sites were cloned from pcDNA3.1-mDsg2-3×Flag (C). Both *Dsg2* cDNA were cloned back into pCDH plasmid containing 3xFlag tag and ampicillin resistance selection marker. These vectors were transformed into DH5α competent cells, and single clones were selected from LB Agar plates to grow in the LB broth. After verification by PCR and DNA sequencing, plasmids were purified using the Plasmid Midi Kit (QIAGEN). Plasmids containing inserted *Dsg2* cDNA were mixed with psPAX-2 and VSVG plasmids at a ratio of 10:3:2, and used to transfect HEK293T cells with EZ Trans reagent. Six hours post-transfection, the culture medium was replaced with fresh DMEM complete culture medium. Virus particles were harvested from the culture medium of HEK 293 T cells after 48 h incubation. The viral medium was mixed with HL-1 cell culture medium at a ratio of 1:1 to transfect the HL-1 cells. After 48 h of lentiviral transfection, fresh HL-1 cell culture medium containing puromycin (2ug mL^{-1}) was used to select HL-1 cells transfected with lentivirus. Stable clones were amplified after 10 days of puromycin selection and were identified by qPCR and immunoblotting.

Knockdown of *Atf4* in HL-1 cells via CRISPR-Cas9

Knockdown of *Atf4* was performed using the CRISPR-Cas9 system. The sgRNA sequence was designed using the online CRISPR guide design software (Benchling, https://www.benchling.com) and synthesized by Songon Biotech (Shanghai). After phosphorylation and annealing, the sgRNA containing the BsmBI restriction site was cloned into the lenti-CRISPRv2-puro vector, followed by transformation into DH5α-competent cells and plasmids purification. The supernatant containing lentivirus particles from HEK293T cells was collected 48 h after co-transfection with lenti-CRISPRv2, psPAX-2 and VSVG plasmids. HL-1 cells were then transfected with the viral supernatant for 48 h and subsequently selected with puromycin (2ug mL^{-1}) for 10 days. The knockdown of *Atf4* was verified by Western blotting.

Primary ventricular myocyte isolation and treatment

Adult mice ventricular myocytes (AMVM) were isolated using Langendorf-free method [26]. Briefly, mice were anesthetized by inhaling 1% to 2% isoflurane/oxygen mixture, and the chest was opened to expose the heart. The descending aorta was cut, followed by injection of 7 ml EDTA buffer into the right ventricular. After isolation of the heart from the chest, 10 ml EDTA buffer, 3 ml perfusion buffer, and 30 to 40 ml collagenase buffer were sequentially injected into the left ventricular at the same site. Both ventricles were gently pulled into 1 mm^3 tiny pieces using forceps, and then the cardiomyocytes were dissociated by gentle trituration. The enzyme activity of collagenase was inhibited by stop buffer, and the cell suspension was passed through a 100-μm filter. The cardiomyocytes were isolated from other non-cardiomyocytes by 4 times gravity settling, which included 3 intermediate calcium reinduction buffers to restore the physiological condition of the cardiomyocytes. The cells in every supernatant were collected as non-cardiomyocytes.

For obtaining neonatal mice ventricular myocytes (NMVM) and fibroblasts, hearts were excised from the 0–3 days old $Dsg2^{WT/WT}$ or $Dsg2^{F536C/F536C}$ mice pups, and rinsed with cold PBS. After removing atria tissue, both ventricular were sheared and digested in 0.25% Trypsin (EDTA free) for 7—9 h at 4 ℃, followed by digestion in DMEM medium supplemented with 0.1% collagenase type-II and 1% BSA for 10 min at 37℃. The buffer solution was then transferred to a tube with DMEM and 10% FBS to stop the digestion. This process was repeated 3–4 times until the cardiac tissue was fully digested. After passing the 100-μm filter, the solution was centrifuged at 800 rpm for 5 min, and the pellet was resuspended in DMEM supplemented with 10% FBS and 1% penicillin/streptomycin. The cells were plated in a 6-cm dish and incubated at 37 °C for 90 min to allow the fibroblasts to adhere. Then the supernatant containing cardiomyocytes was collected, plated in 12-well culture plate at $1*10^6$ cells per well, and maintained in medium containing DMEM, M199, 10% FBS, 1% penicillin/streptomycin, and 100 μM 5-Bromo-2'-deoxyuridine for further study. For the p-PERK inhibition assay, NMVMs from $Dsg2^{F536C/F536C}$ mice were treated with GSK2606414 for 24 h, subsequently maintained in normal culture medium for 24 h, and subjected to protein assay. For adenovirus transfection, NMVMs were transfected adenovirus for 12 h, subsequently maintained in normal culture medium for 24 h and subjected to protein assay.

Immunoblotting, immunoprecipitation and mass spectrometry

Heart tissue samples and cells sample were lysed with RIPA buffer (Cell Signaling Technology) supplemented with protease and phosphatase inhibitor cocktail (Roche). The protein fractions were separated by centrifugation and the concentrations were determined by the Pierce BCA kit (Pierce). Protein denaturation was achieved by mixing with Laemmli sample buffer supplemented with 10% β-mercaptoethanol (Sigma-Aldrich) and boiled. Equal amounts of protein extracts were loaded and electrophoresed on SDS–polyacrylamide gels, followed by blotting onto pre-equilibrated Immobilon-P polyvinylidene fluoride membrane (Millipore). The protein fractions were probed with primary antibodies overnight at 4 °C, followed by incubation with HRP-conjugated secondary antibody. The bands were detected using Super-Signal West Femto substrate (Pierce) on a ChemiDoc Imaging system (Bio-Rad). Band intensity quantification was performed using ImageJ. To identify ubiquitination of vDSG2, immunoprecipitation with anti-Flag antibody was conducted in HL-1 cells with stable expression of vDSG2 and wtDSG2. HL-1 cells were lysed with IP lysis buffer (Pierce) supplemented with protease and phosphatase inhibitor cocktail (Roche). Lysates were separated by centrifugation, and the supernatants were incubated with anti-Flag antibody and tumbled overnight at 4 °C. Protein A agarose beads (Cell Signaling Technology) were then added into the lysates, and tumbled for 2 h at 4 °C. After being rinsed with IP lysis buffer five times, the bead-bound proteins were solubilized with Laemmli sample buffer supplemented with 10% β-mercaptoethanol and boiled to denature, followed by immunoblotting to probe the target protein.

To screen for potential vDSG2-interacting proteins, cell lysates purified by immunoprecipitation with anti-Flag antibody in HL-vDSG2 cells were loaded onto SDS-PAGE gels and stained with Coomassie Brilliant Blue (Beyotime). Bands were exercised from the gel, digested, and subjected to mass spectrometry analysis via online nano-reversed phase liquid chromatography (Oebiotech). The MS/MS data were analyzed using ProteomeDiscoverer 2.5.

Quantitative real-time polymerase chain reaction (qPCR)

Total RNA samples were extracted from mouse heart tissue and HL-1 cells using Trizol reagent (Invitrogen) and the RNeasy Mini Kit (Qiagen) following the manufacturer's instructions. A total of 1000 ng mRNA was used to synthesize cDNA using iScript reagent (Bio-Rad). Quantitative PCR (qPCR) was performed using SYBR Green mix (Bio-Rad). The $2^{-\Delta\Delta CT}$ method was employed to estimate the mRNA levels of target genes, calculating fold changes relative to the expression of GAPDH or β-actin, which served as endogenous controls.

RNA-sequencing and data analysis

Bulk RNA-sequencing (RNA-Seq) was conducted to explore the potential mechanisms underlying the pathogenesis of ACM caused by $Dsg2^{F536C}$. Total RNA was extracted from the hearts of $Dsg2^{F536C/F536C}$, $Dsg2^{F536C/WT}$, and $Dsg2^{WT/WT}$ mice at 10 weeks of age. Sequencing was performed on the Hiseq-PE150 instrument using paired-end sample preparation chemistry. The raw RNA-Seq reads were aligned to the mm10 genome using Hisat2 (version 2.1.0) with parameters '–no-unal –no-mixed –no-discordant'. Gene count values were quantified using Featurecounts (version 2.0.0). Gene transcript per million (TPM) values were generated by custom R scripts. DESeq2 (version 1.28.1) was utilized for differential analyses with cutoffs FoldChange > = 2 and adjusted P value < = 0.05. Gene ontology (GO) analysis for differentially expressed genes was performed using DAVID (version 6.8). Gene Set Enrichment Analysis (GSEA) employed the 'GSEA' function of the clusterProfiler R package (version 4.6.0).

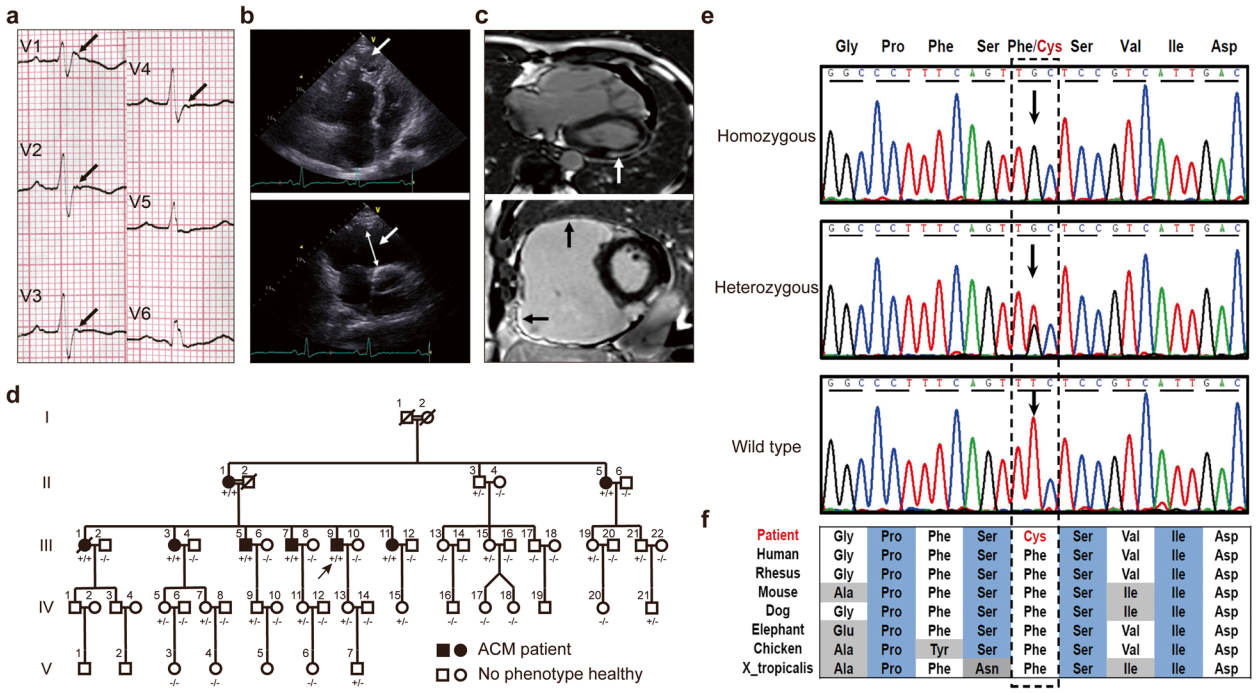

Fig. 1 Clinical characteristics and the family pedigree of the patients with the c.1592 T > G (p.Phe531Cys) variant in *DSG2*. **a** Conventional electrocardiography showed T-wave inversion and epsilon waves (black arrows) in the precordial leads. **b** Transthoracic echocardiography showed thinning of the apical myocardium of the right ventricle, the formation of aneurysm (arrow in the upper figure), and the widening of right ventricular outflow tract (arrow in the lower figure). **c** Fibrosis in both the left ventricle (arrow in the upper figure) and right ventricle (arrow in the lower figure) identified by cardiac LGE + MRI. **d** Family pedigree of the ACM patients with the c.1592 T > G (p.Phe531Cys) variant in *DSG2*. The filled symbols represented clinically diagnosed ACM patients, and open symbols were heathy individuals without clinical characteristics of ACM. The proband was marked with an arrow ((III-9)). **e** Sanger sequencing was performed to validate the variant identified by targeted sequencing and whole-exome sequencing. **f** The variant (F531C) was located in an evolutionary highly conservative area across multiple species

snRNA-seq analysis

An available processed single-nucleus RNA sequencing (snRNA-seq) dataset containing human ACM and normal heart tissues was downloaded from CellxGene (https://cellxgene.cziscience.com/collections/e75342a8-0f3b-4ec5-8ee1-245a23e0f7cb) [27]. Cardiac cell types were already well-clustered and annotated in the study, and we used the annotations directly from the dataset's metadata. Data from normal ventricular tissues was extracted and visualized with Dimplot using Seurat (4.2.0). The expression levels of *DSG2* in different cell clusters were showed with FeaturePlot and VlnPlot.

Statistical analysis

Continuous variables are presented as mean ± standard deviation. The Shapiro–Wilk normality test was utilized to assess data distribution. For normally distributed data, unpaired t-tests (for two datasets) or one-way ANOVA with Tukey's multiple comparison test (for three datasets) was employed. Alternatively, the Mann–Whitney U test (for two datasets) or Kruskal–Wallis test with Dunn's multiple comparison test (for three datasets) was were used for non-normally distributed data. All data were processed and analyzed using GraphPad Prism 8.0.2, with significance set at a two-tailed p-value < 0.05.

Results

Identifying *DSG2*^{F531C} variant in an ACM family

Clinical evaluations were performed systematically for all family members, eight of whom were diagnosed with ACM according to the updated diagnostic criteria for ACM [20, 21]. All patients with ACM presented with palpitations and dyspnea, and the eldest sister of the index patient died suddenly at the age of 50 (III-1) (Additional file 2: Table S1). The mean age of onset of symptomatic ACM was 50.5 ± 6.38 years. Typical characteristics of surface ECG in patients with ACM include complete right bundle branch block, prolonged terminal activation duration of QRS (≥ 55 ms) in lead V1-V3, typical epsilon wave, abnormal inverted T-waves in precordial leads (Fig. 1a, Additional file 2: Table S1), and frequent ventricular premature complex and/or ventricular tachycardia with left bundle branch block morphology (Additional file 1: Fig. S1, Additional file 2: Table S1).

Echocardiographic findings indicated diffuse right ventricular dilation and regional akinesia or aneurysm in the right ventricular free wall in all patients with ACM, three of whom had abnormalities in the left ventricle (II-1, III-3, and III-9) (Fig. 1b, Additional file 2: Table S1). Cardiac MRI revealed a paradoxical movement of the apical myocardium of the right ventricle, systolic myocardial ectasia, aneurysm formation in the right ventricle, and fibrosis in both ventricles (Fig. 1c, Additional file 2: Table S1).

The grandparents (I-1 and I-2) and parents (II-I & II-2) of the proband were consanguineous (Fig. 1d). We identified a homozygous *DSG2* missense variant, c.1592 T > G, in the proband (III-9, Fig. 1d, e). This missense variant leads to an amino acid change p.F531C, which is considered detrimental according to PolyPhen-2 and SIFT analyses. This variant was observed in 0.093% of alleles (heterozygous state) from individuals of East Asian descent in the Exome Aggregation Consortium. In addition, we identified only one heterozygous $DSG2^{F531C}$ variant among 950 healthy controls. Bioinformatic analysis confirmed that the amino acid at the variant site was highly conserved among DSG2 homologs in lower organisms and vertebrates, and even in other members of the cadherin family (Fig. 1f, Additional file 1: Fig. S2a). Furthermore, whole-exome sequencing in the proband revealed no additional pathogenic or likely pathogenic variants associated with ACM. In addition, we performed cascade screening of the remaining family members. Interestingly, all the family members diagnosed with ACM were homozygous carriers of this variant. All heterozygous carriers (12 members) were absent from the ACM clinical characteristics (Fig. 1d, Additional file 2: Table S1).

Homozygous $Dsg2^{F536C}$ mice presented with cardiac enlargement, systolic dysfunction, and progressive cardiac fibrosis

Phenylalanine at the 536th position of mouse DSG2 was homologous to phenylalanine at the 531st position of human DSG2 (Additional file 1: Fig. S2b). Therefore, we generated $Dsg2^{F536C}$ knock-in mice using homologous recombination technology to validate the pathogenicity of $Dsg2^{F536C}$ variant and investigate its mechanism in ACM pathogenesis (Additional file 1: Fig. S3). Echocardiography was performed to assess the cardiac geometry and function in homozygous $Dsg2^{F536C/F536C}$, heterozygous $Dsg2^{F536C/WT}$, and $Dsg2^{WT/WT}$ mice at 10 weeks of age, which were considered adult mice. Left ventricular ejection fraction and left ventricular fractional shortening were markedly lower in $Dsg2^{F536C/F536C}$ mice than in $Dsg2^{WT/WT}$, accompanied by an increased left ventricular internal diameter (Fig. 2a, b). In addition, the left ventricular wall thickness was lower in $Dsg2^{F536C/F536C}$ mice (Additional file 1: Fig. S4). These findings indicated that $Dsg2^{F536C/F536C}$ mice had abnormalities in cardiac geometry and function. Electrocardiography showed increased P-wave duration and amplitude in $Dsg2^{F536C/F536C}$ mice at 10 weeks of age as well as prolonged QRS duration and decreased QRS amplitude (Fig. 2c, d), implying depolarization and conduction abnormalities in $Dsg2^{F536C/F536C}$ mice. No differences in echocardiography or electrocardiography were observed between $Dsg2^{WT/WT}$ and $Dsg2^{F536C/WT}$ mice (Fig. 2a-d, Additional file 1: Fig. S4).

The loss of cardiomyocytes and replacement of fibrous tissue are the most important hallmarks of ACM pathology. Masson's trichrome staining demonstrated obvious fibrotic infiltration in both ventricles of $Dsg2^{F536C/F536C}$ mice (Fig. 2e). The CVF of hearts from $Dsg2^{F536C/F536C}$ mice was significantly higher than that of hearts from $Dsg2^{F536C/WT}$ and $Dsg2^{WT/WT}$ mice (Fig. 2f). Fibrosis was mainly located at the free wall of both ventricles, but less so in the interventricular septum (Fig. 2f). The free walls of both ventricles in $Dsg2^{F536C/F536C}$ mice were significantly thinner than those in $Dsg2^{F536C/WT}$ and $Dsg2^{WT/WT}$ mice (Fig. 2g). Furthermore, we examined the fibrosis patterns in the hearts of $Dsg2^{F536C/F536C}$ mice. Replacement fibrosis secondary to cardiomyocyte loss, interstitial fibrosis, and perivascular fibrosis were all evident

(See figure on next page.)

Fig. 2 Homozygous $Dsg2^{F536C}$ mice had cardiac enlargement, systolic dysfunction, and progressive cardiac fibrosis. **a** Representative images of M-mode echocardiography in 10-week-old $Dsg2^{WT/WT}$ (WT), $Dsg2^{F536C/WT}$ (Het) and $Dsg2^{F536C/F536C}$ (Hom) mice. **b** Quantification analysis of LV geometry (LVDD and LVDS) and systolic function (LVEF and LVFS) among 10-week-old WT, Het and Hom mice. $N = 13$ in WT group, $N = 16$ in Het group, and $N = 19$ in Hom group. **c** Representative images of ECG recorded in 10-week-old WT, Het and Hom mice. **d** Quantification of the duration and amplitude of P wave and QRS complex among 10-week-old WT, Het and Hom mice. $N = 6$ in each group. **e** Representative images of Masson's staining in 10-week-old WT, Het and Hom mice. $N = 6$ in each group. **f** Quantification of cardiac collagen volume fraction in 10-week-old WT, Het and Hom mice. **g** Quantification of thickness of both free ventricular walls in 10-week-old WT, Het and Hom mice. **h** Representative images of cardiac replacement fibrosis, interstitial fibrosis, and perivascular fibrosis in 10-week-old Hom mice. **i** Representative images of cardiac progressive fibrosis in Hom mice. **j** Quantification of cardiac collagen volume fraction in Hom mice from 2-week-old to 10-week-old ($N = 5$ in each group). ***: $p < 0.001$ compared with the hearts from 2-week-old mice, ###: $p < 0.001$ compared with the hearts from 4-week-old mice. **k** Quantification of ventricular wall thickness in Hom mice from 2-week-old to 10-week-old ($N = 5$ in each group). * $p < 0.05$ compared with the hearts from 2-week-old mice, ** $p < 0.01$ compared with the hearts from 2-week-old mice, ***: $p < 0.001$ compared with the hearts from 2-week-old mice, ###: $p < 0.001$ compared with the hearts from 4-week-old mice. Ordinary one-way ANOVA with Turkey's multiple comparisons test was used to analyze the data

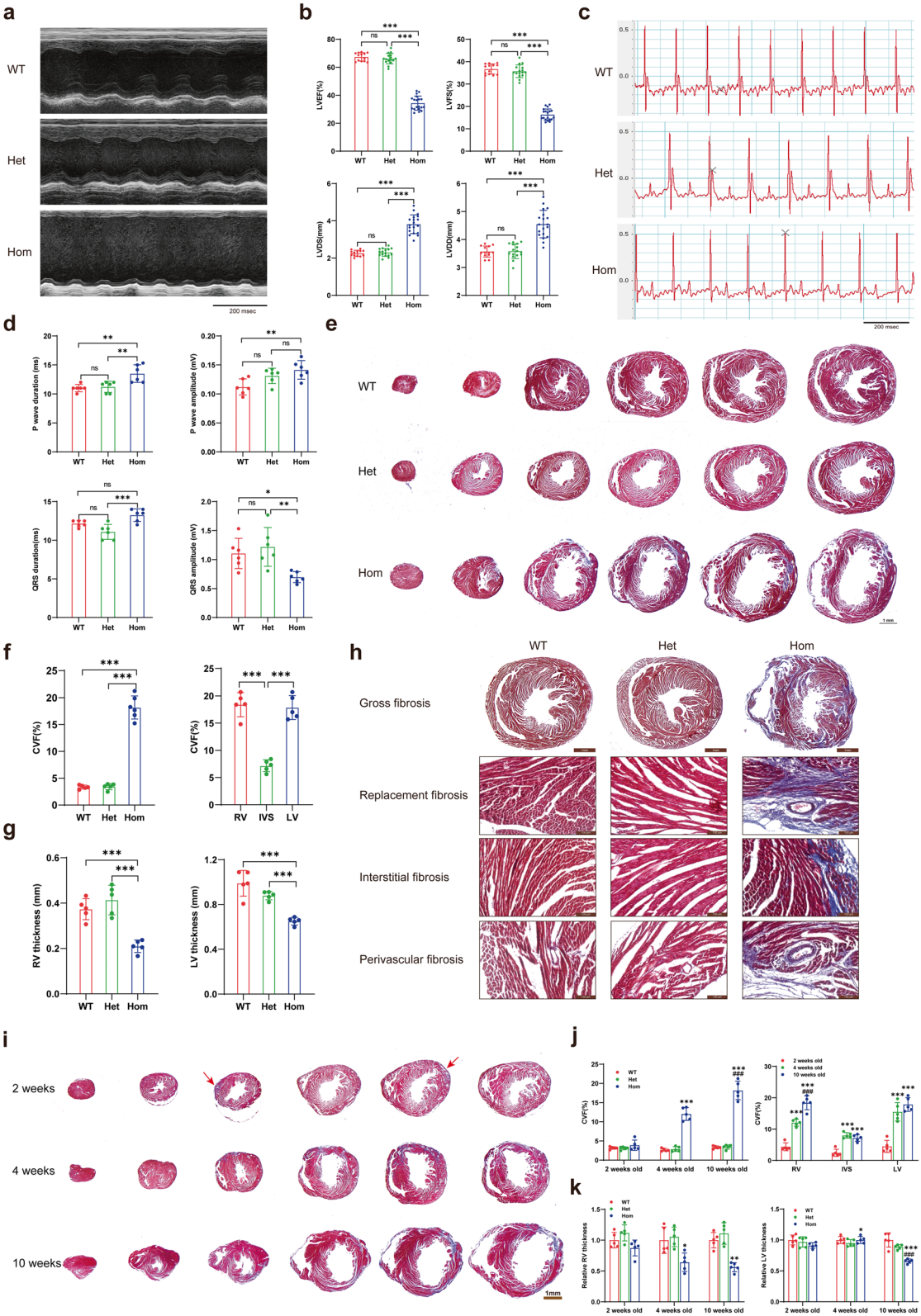

Fig. 2 (See legend on previous page.)

in the hearts of $Dsg2^{F536C/F536C}$ mice (Fig. 2h). To clarify the disease course and progression of ACM, hearts from $Dsg2^{F536C/F536C}$, $Dsg2^{F536C/WT}$ and $Dsg2^{WT/WT}$ mice at early stages (2 and 4 weeks) were excised for Masson's trichrome staining. Obvious fibrosis was observed in both ventricles of 4-week-old $Dsg2^{F536C/F536C}$ mice (Fig. 2i, Additional file 1: Fig. S5a). Unexpectedly, fibrosis was observed in some $Dsg2^{F536C/F536C}$ mice at 2 weeks of age and was locally scattered in the epicardium of both ventricles (Fig. 2i). Therefore, cardiac fibrosis in $Dsg2^{F536C/F536C}$ mice had several characteristics: presence at a very early stage (2 weeks), early involvement of both ventricles, rapid progression from the epicardium to the endocardium (Fig. 2i, j). In addition, the thicknesses of both ventricles in $Dsg2^{F536C/F536C}$ mice decreased progressively (Fig. 2k, Additional file 1: Fig. S5c). Consistent with the echocardiography and electrocardiography results, no pathological characteristics of ACM were observed in the hearts of $Dsg2^{F536C/WT}$ mice, indicating that heterozygous $Dsg2^{F536C}$ carriers might be exempt from ACM.

Both the pedigree investigation and animal study showed that ACM was absent in heterozygous $DSG2^{F531C}$ carriers, which differed from most desmosome gene-related ACM cases [28]. To confirm this finding, a pharmacological stress study with isoproterenol (ISO) intraperitoneal injection (20 mg Kg^{-1} body weight for 2 weeks), which was used to increase mechanical stress and accelerate the progression of ACM [29], was performed in $Dsg2^{F536C/WT}$ and $Dsg2^{WT/WT}$ mice (Additional file 1: Fig. S6a). Although echocardiography results showed impaired cardiac systolic function after a two-week ISO injection, the changes were similar between $Dsg2^{F536C/WT}$ and $Dsg2^{WT/WT}$ mice (Additional file 1: Fig. S6b, c). Interstitial fibrosis induced by ISO was observed in the hearts of both $Dsg2^{F536C/WT}$ and $Dsg2^{WT/WT}$ mice, but there was no significant difference in the cardiac fibrosis between the two groups (Additional file 1: Fig. S6d, e). In addition, the distribution of cardiac fibrosis induced by ISO in $Dsg2^{F536C/WT}$ mice was mainly in the endocardium and septum, which was different from that in $Dsg2^{F536C/F536C}$ mice, but was similar to the distribution of cardiac fibrosis in WT mice treated with ISO (Additional file 1: Fig. S6d, e). In addition, there were no significant differences in the thickness of either ventricle between $Dsg2^{F536C/WT}$ and $Dsg2^{WT/WT}$ mice (Additional file 1: Fig. S6d, e). Therefore, fibrosis in the hearts of $Dsg2^{F536C/WT}$ mice was due to the direct pro-fibrotic effects of ISO [30], which was also present in WT mice. These results indicate that ACM was absent from heterozygous $DSG2^{F531C}$ variant carriers, even under severe mechanical stress and sympathetic hyperactivity.

DSG2-F536C was degraded through the ubiquitin–proteasome system

Western blotting and immunohistochemistry were performed to investigate the effect of the variant on the level and location of DSG2. Unexpectedly, there was nearly undetectable DSG2 in immunoblotting in hearts from $Dsg2^{F536C/F536C}$ mice (Fig. 3a). Immunohistochemistry demonstrated that DSG2 mainly located at desmosomes in the hearts from $Dsg2^{WT/WT}$ and $Dsg2^{F536C/WT}$ mice, but was absent in $Dsg2^{F536C/F536C}$ mice (red arrow in Fig. 3b). The levels of *Dsg2* mRNA from the hearts of $Dsg2^{F536C/F536C}$ mice were similar to those in $Dsg2^{F536C/WT}$ and $Dsg2^{WT/WT}$ mice (Additional file 1: Fig. S7a), excluding the possibility of abnormal transcription or degradation of the variant *Dsg2* mRNA. The overexpression of vDSG2, tagged with a C-terminal 3xFlag, in HEK293T cells effectively ruled out the possibility that the antibody was unable to recognize vDSG2 (Additional file 1: Fig. S7b). We speculated that vDSG2 might be modified and degraded after translation. 3D models of wtDSG2 and vDSG2 protein were constructed using AlphaFold2 [31]. Root Mean Square Deviation (RMSD) was used to quantify the differences between the structure of wtDSG2 and vDSG2. Although there was no significant change in protein structure at the variant site (RMSD = 0.876), the global structure of vDSG2 was significantly altered (RMSD 16.679, Fig. 3c, Additional file 1: Fig. S7c). Further comparison of the three-dimensional structures of

(See figure on next page.)

Fig. 3 DSG2-F536C was degraded via ubiquitin–proteasome system. **a** Representative western blot and quantification of DSG2 protein levels in the hearts from 10-week-old $Dsg2^{WT/WT}$ (WT), $Dsg2^{F536C/WT}$ (Het) and $Dsg2^{F536C/F536C}$ (Hom) mice. $N = 6$ in each group. **b** Representative images of immunohistochemical staining and quantification of DSP and DSG2 in the hearts of 10-week-old WT, Het, and Hom mice. **c** The predicted 3D model of wild-type DSG2 protein (left) and the variant DSG2-F536C protein (right) via AlphaFold2. **d** Representative western blot and quantification of DSG2-Flag protein levels in HL-1 cells (Ctrl), HL-1 cells with stable expression of vDSG2 (vDSG2), and HL-1 cells with stable expression of wtDSG2 (wtDSG2). $N = 3$ in each group. **e** Mass spectrometry analysis revealed several candidates interacting with vDSG2. **f** Representative western blot and quantification of the ubiquitination of DSG2-Flag followed immunoprecipitation with anti-Flag antibody. $N = 3$ in each group. **g** Representative western blot and quantification of DSG2-Flag protein levels in HL-1 cells with stable expression of vDSG2 treated with DMSO, MG132 (10 μM for 8 h), or CQ (25 μM for 8 h). $N = 3$ in each group. **h** Representative western blot and quantification of DSG2-Flag in HL-1 cells with stable expression of vDSG2 or vDSG2 with lysine site mutation. $N = 3$ in each group. Ordinary one-way ANOVA with Turkey's multiple comparisons test or Unpaired t-test were used to analyze the data, * $p < 0.05$, **: $p < 0.01$, ***: $p < 0.001$

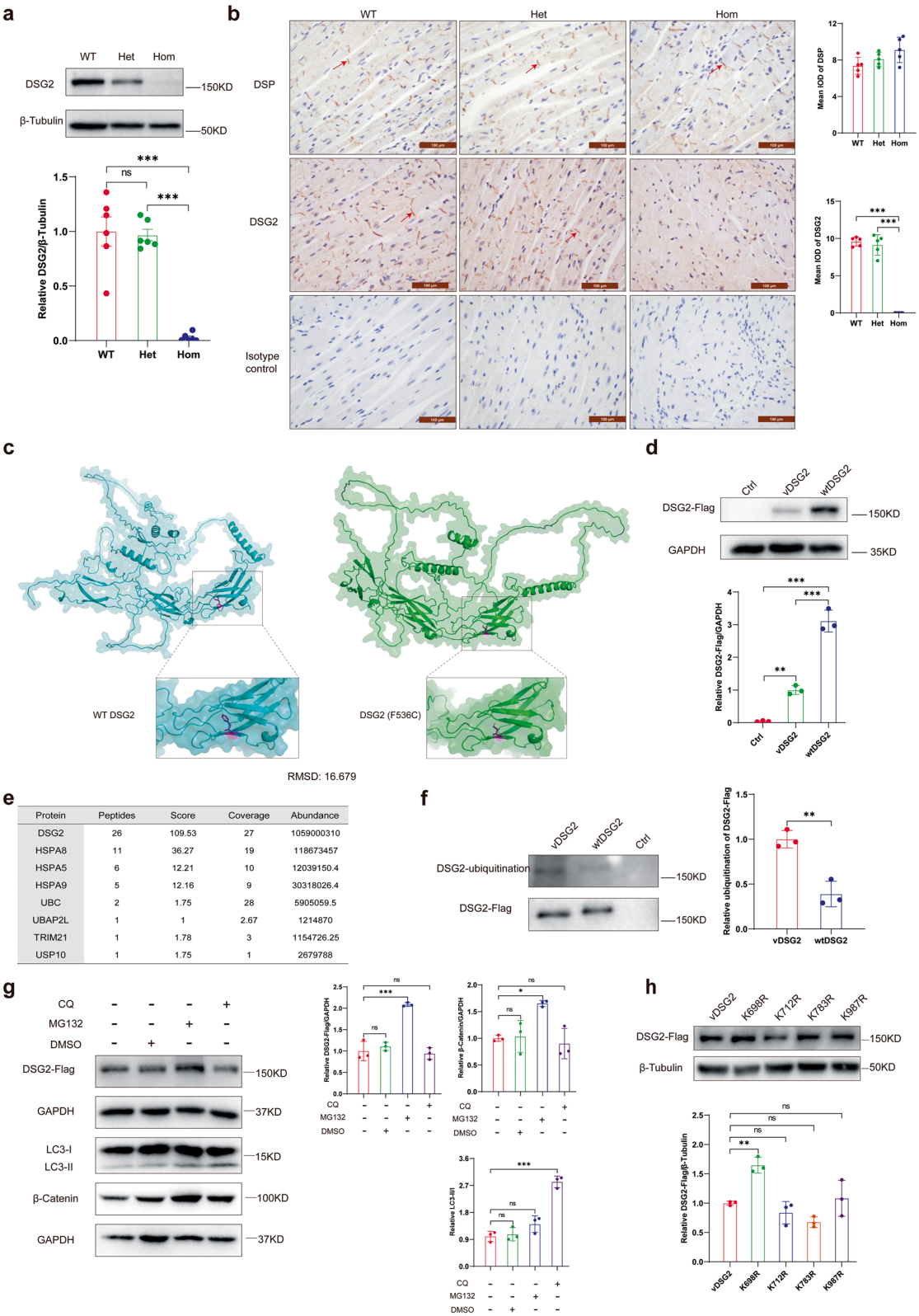

Protein	Peptides	Score	Coverage	Abundance
DSG2	26	109.53	27	1059000310
HSPA8	11	36.27	19	118673457
HSPA5	6	12.21	10	12039150.4
HSPA9	5	12.16	9	30318026.4
UBC	2	1.75	28	5905059.5
UBAP2L	1	1	2.67	1214870
TRIM21	1	1.78	3	1154726.25
USP10	1	1.75	1	2679788

Fig. 3 (See legend on previous page.)

vDSG2 and wtDSG2 revealed abnormal folding in the intracellular segment (amino acids 630–781) of vDSG2 (red segment in vDSG2 and yellow segment in wtDSG2 in Additional file 1: Fig. S7d). To validate the degradation of vDSG2 in cardiomyocytes, HL-1 cells with stable expression vDSG2-Flag (HL-vDSG2) and wtDSG2-Flag (HL-wtDSG2) were generated by lentiviral transfection and puromycin screening. The mRNA levels of *Dsg2* were similar between HL-vDSG2 and HL-wtDSG2 cells (Additional file 1: Fig. S7e), but the protein levels of DSG2-Flag in HL-vDSG2 cells were significantly decreased (Fig. 3d), which was in accordance with the nearly undetectable DSG2 in the hearts from $Dsg2^{F536C/F536C}$ mice.

Mass spectrometry analysis of proteins purified by immunoprecipitation with an anti-Flag antibody in HL-vDSG2 cells showed that ubiquitination-related proteins (UBC, UBAP2L, TRIM21, USP10) were potential candidates interacting with vDSG2 (Fig. 3e, Additional file 3: Table S2), suggesting that vDSG2 might be modified by ubiquitin in cardiomyocytes. The ubiquitin–proteasome system (UPS) and autophagy-lysosome system are the major pathways for clearing misfolded and aggregation-prone proteins in cardiomyocytes [32]. We purified DSG2-Flag via immunoprecipitation with an anti-Flag antibody in HL-1, HL-vDSG2, and HL-wtDSG2 cells to compare the ubiquitination levels between vDSG2 and wtDSG2. There was a robust increase in the ubiquitination of vDSG2 compared to that of wtDSG2 (Fig. 3f). HL-vDSG2 cells were then treated with proteasome inhibitor (MG-132) and lysosomal inhibitor (chloroquine, CQ). The levels of DSG2-Flag increased significantly with MG-132 treatment but remained unchanged after CQ treatment (Fig. 3g). In contrast, the DSG2-Flag levels in HL-wtDSG2 cells did not increase after MG-132 treatment (Additional file 1: Fig. S7f). These results validated that UPS contributed to the degradation of the DSG2-F536C variant protein in cardiomyocytes.

Four lysines in mouse DSG2 (K698, K712, K783, and K987) were predicted to be modified by ubiquitin using PhosphoSitePlus. Each predicted lysine was mutated to an arginine to identify the ubiquitination sites involved in the degradation of vDSG2. The K698R mutation attenuated the degradation of vDSG2 in HL-vDSG2 cells (Fig. 3h), indicating that K698 is the ubiquitination site contributing to the degradation of vDSG2.

Primary activation of TGF-β1/SMADs signaling in the hearts from $Dsg2^{F536C/F536C}$ mice

Degradation of the DSG2-F536C variant protein via the UPS may impair the desmosome structure and function, a common mechanism underlying ACM caused by desmosomal genetic variations, which is insufficient to match the high risk of progressive heart failure in ACM caused by *DSG2* variants. RNA sequencing of bulk hearts was performed to investigate the potential unique mechanisms underlying the pathogenesis of ACM caused by $Dsg2^{F536C}$. Generally, the transcriptome of $Dsg2^{F536C/F536C}$ mice showed significant differences compared with $Dsg2^{F536C/WT}$ mice and $Dsg2^{WT/WT}$ mice (Additional file 1: Fig. S8a). Of the 878 differentially expressed genes (DEGs) between $Dsg2^{F536C/F536C}$ and $Dsg2^{F536C/WT}$ mice, 753 genes were upregulated and 125 genes were downregulated in $Dsg2^{F536C/F536C}$ mice. Of the 1230 DEGs between $Dsg2^{F536C/F536C}$ and $Dsg2^{WT/WT}$ mice, 1074 genes were upregulated and 156 genes were downregulated in $Dsg2^{F536C/F536C}$ mice. However, there were only 3 DEGs between $Dsg2^{F536C/WT}$ and $Dsg2^{WT/WT}$ mice (Additional file 1: Fig. S8b-c), providing molecular evidence for the absence of ACM in $Dsg2^{F536C/WT}$ mice. Furthermore, 630 genes were upregulated in $Dsg2^{F536C/F536C}$ mice compared with both $Dsg2^{F536C/WT}$ and $Dsg2^{WT/WT}$ mice (Additional file 1: Fig. S8c). GO analyses showed that genes with increased expression were enriched for functional terms related with inflammatory response, cell adhesion, extracellular remodeling and cellular response to transforming growth factor beta stimulus (Additional file 1: Fig. S8d). Given that cardiac fibrosis is the primary pathological feature of ACM mice and considering the central role of the TGF-β signaling pathway in cardiac fibrosis, we further confirmed the activation of the TGF-β1 signaling pathway in the hearts of $Dsg2^{F536C/F536C}$ mice through GSEA (Fig. 4a-c, Additional file 4). Western blotting showed markedly increased levels of TGF-β1 in $Dsg2^{F536C/F536C}$ hearts compared to those in $Dsg2^{WT/WT}$ and $Dsg2^{F536C/WT}$ hearts (Fig. 4d) as well as elevated phosphorylation levels of SMAD2/3 (Fig. 4e, f). These results indicated that the canonical TGF-β1 pathway was activated and might be an important mechanism in ACM.

As the master regulator of fibrosis, TGF-β1 plays a pivotal role in cardiac fibrosis and is upregulated under stress, inflammation, fibrosis, and myocardial injury [33]. The elevated TGF-β1 may be the primary cause or secondary effect of cardiac fibrosis in 10-week-old $Dsg2^{F536C/F536C}$ mice. We compared TGF-β1 levels in the hearts of $Dsg2^{F536C/F536C}$, $Dsg2^{F536C/WT}$ and $Dsg2^{WT/WT}$ mice at 1 week of age, when cardiac fibrosis was absent in $Dsg2^{F536C/F536C}$ mice. The results showed a trend of elevated TGF-β1 expression in the hearts of $Dsg2^{F536C/F536C}$ mice before the onset of fibrosis (Additional file 1: Fig. S8e). Furthermore, TGF-β1 levels in NMVM from $Dsg2^{F536C/F536C}$ mice were significantly increased, but were similar between neonatal mouse cardiac fibroblasts from $Dsg2^{F536C/F536C}$ and $Dsg2^{WT/WT}$ mice (Fig. 4g). A previous dataset found that *DSG2* was mainly expressed in human cardiomyocytes, but not in fibroblasts

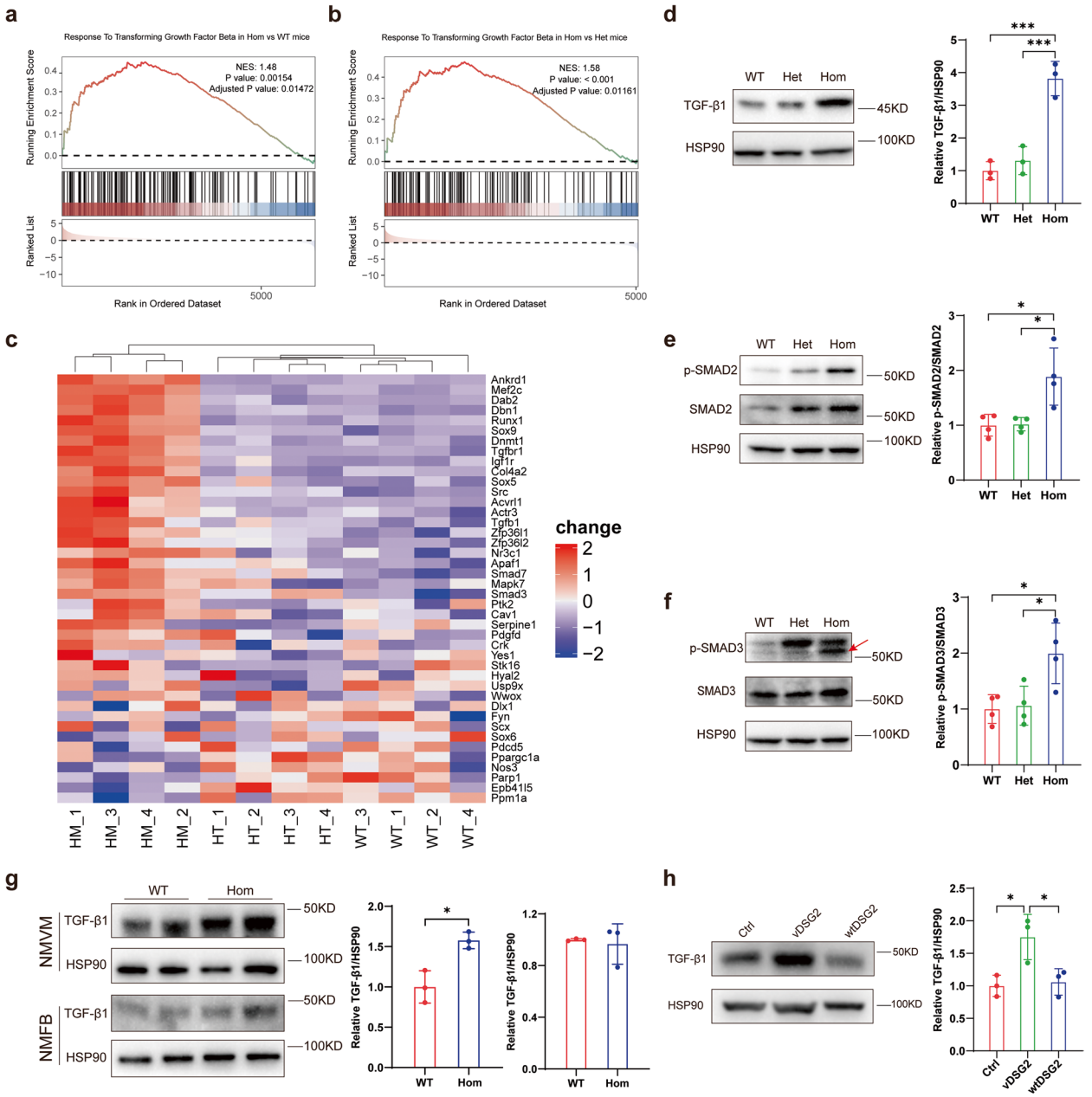

Fig. 4 Primary activation of TGF-β1/SMADs signaling in hearts from *Dsg2*$^{F536C/F536C}$ mice. **a-b** GSEA indicated that response to TGF-beta stimulus pathway was activated in the hearts in 10-week-old *Dsg2*$^{F536C/F536C}$ (Hom) mice compared with *Dsg2*$^{WT/WT}$ (WT) or *Dsg2*$^{F536C/WT}$ (Het) mice. **c** Heatmap of DEGs in cellular response to TGF-beta stimulus pathway. **d** Representative western blot and quantification of TGF-β1 protein levels in the hearts from 10-week-old WT, Het and Hom mice. $N=4$ in each group. **e–f** Representative western blot and quantification of the ratio of p-SMAD2/SMAD2 (**e**) and p-SMAD3/SMAD3 (**f**) in the hearts from 10-week-old WT, Het and Hom mice. $N=4$ in each group. **g** Representative western blot and quantification of TGF-β1 protein levels in NMVM and NMFB from WT and Hom mice. $N=3$ in each group. **h** Representative western blot and quantification of TGF-β1 protein levels in HL-1 cells (Ctrl), HL-1 cells with stable overexpression of variant DSG2 (vDSG2) and HL-1 cells with stable overexpression of wild-type DSG2 (wtDSG2). $N=3$ in each group. Mann–Whitney U test was used to investigate the difference of TGF-β1 in NMFB between WT and Hom mice in panel g. Otherwise, ordinary one-way ANOVA with Turkey's multiple comparisons test or Unpaired t-test were used to analyze the data, * $p<0.05$, **: $p<0.01$, ***: $p<0.001$

(Additional file 1: Fig. S9a-c) [27]. Immunoblotting also showed undetectable DSG2 levels in cardiac fibroblasts isolated from neonatal rats (Additional file 1: Fig. S9d). Together, these results suggested that elevated TGF-β1 levels in the hearts from *Dsg2*$^{F536C/F536C}$ mice might be directly due to the DSG2-F536C variant protein in

cardiomyocytes, which was further corroborated in HL-vDSG2 cells (Fig. 4h).

Cardiac fibroblast activation and differentiation into myofibroblasts are hallmarks of cardiac fibrosis [34]. Due to the low expression of DSG2 in cardiac fibroblasts, we hypothesized that cardiac fibroblasts were passively activated by TGF-β1 released by cardiomyocytes in *Dsg2*$^{F536C/F536C}$ mice. To investigate this, we treated neonatal mouse cardiac fibroblasts with conditioned medium from HL-1, HL-vDSG2 and HL-wtDSG2 cells, respectively. We observed enhanced migration ability (Additional file 1: Fig. S9e), increased expression of α-SMA (Additional file 1: Fig. S9f), and activation of the canonical TGF-β1/SMADs signaling (Additional file 1: Fig. S9g, h) in cardiac fibroblasts treated with conditioned medium from HL-vDSG2 cells. These results indicated that increased levels of TGF-β1 in cardiomyocytes could activate cardiac fibroblasts and promote cardiac fibrosis through paracrine signaling.

DSG2-F536C promoted TGF-β1 expression by inducing endoplasmic reticulum stress in cardiomyocytes

The mechanism underlying the increased expression of TGF-β1 induced by the DSG2-F536C variant in cardiomyocytes remains unclear. Mass spectrometry analysis showed that HSPA5 (also known as BiP) might interact with vDSG2 (Fig. 3e, Additional file 3: Table S2), which was validated by co-immunoprecipitation (Co-IP) (Fig. 5a). As an important chaperone, BiP is responsible to bind with misfolded protein in ER. The interaction between vDSG2 and BiP indicated that vDSG2 entered into the ER, and was recognized as misfolded protein. The interaction between BiP and misfolded protein could induce ER stress and activate the UPR. Increased levels of BiP in NMVM from *Dsg2*$^{F536C/F536C}$ mice, as well as in HL-vDSG2 cells, implied that the DSG2-F536C variant protein could induce ER stress in cardiomyocytes (Fig. 5b, Additional file 1: Fig. S10a). Elevated levels of BiP and C/EBP homologous protein (CHOP) were also observed in the cardiac tissue of 1-week and 10-week-old *Dsg2*$^{F536C/F536C}$ mice (Fig. 5c, d), providing evidence of ER stress in the hearts of *DSG2*$^{F536C/F536C}$ mice. Cytoskeleton associated protein 4 (CKAP4), a marker protein of sheet-like cisternal ER [35], was shown to be increasingly expressed in the hearts of 10-week-old *Dsg2*$^{F536C/F536C}$ mice, presenting with an increased intensity and area of CKAP4 in cardiomyocytes on immunofluorescence staining (Fig. 5e). Immunoblotting also revealed increased CKAP4 levels in the hearts of 10-week-old *Dsg2*$^{F536C/F536C}$ mice (Fig. 5f). These results indicated ER expansion in cardiomyocytes from *Dsg2*$^{F536C/F536C}$ mice, which is an important characteristic of ER stress [36]. Furthermore, immunoblotting revealed that BiP levels were significantly higher in adult mouse ventricular myocytes than in non-cardiomyocytes (Fig. 5g), supporting that ER stress induced by vDSG2 was mainly in cardiomyocytes.

To investigate the relationship between ER stress and elevated TGF-β1 in cardiomyocytes, HL-1 cells were treated with brefeldin A (BFA) to induce ER stress. The findings revealed elevated TGF-β1 levels in BFA-treated cardiomyocytes compared to those in control cells (Additional file 1: Fig. S10b). Furthermore, by overexpressing BiP to inhibit ER stress in HL-vDSG2 cells [37], we observed a reduction in the expression of TGF-β1 (Fig. 5h). These results demonstrated that ER stress could promote the expression of TGF-β1 in cardiomyocytes.

DSG2-F536C promoted the expression of TGF-β1 via the PERK-ATF4 signaling in cardiomyocytes

There are three pathways of UPR in mammals: PERK-ATF4, IRE1-XBP1s, and ATF6 signaling (Fig. 6a) [38]. Considering that ATF4, XBP1s, and cleaved ATF6 are the main transcription factors downstream of the UPR pathway, we assessed the protein levels of these transcription factors in HL-vDSG2 cells. Immunoblotting showed increased levels of ATF4 (Fig. 6b), unchanged levels of XBP1s, and decreased levels of cleaved ATF6 in HL-vDSG2 cells (Additional file 1: Fig. S11a). Immunoblotting of cardiac tissue also showed that only ATF4 levels were significantly increased in 10-week-old *Dsg2*$^{F536C/F536C}$ mice (Fig. 6d, Additional file 1: Fig. S11b). In addition, the ratios of phosphorylated PERK (p-PERK)/PERK and p-eIF2α/eIF2α in both HL-vDSG2 cells and cardiac tissue from 10-week-old *Dsg2*$^{F536C/F536C}$ mice were increased parallelly (Fig. 6c, d). These results demonstrate that only the PERK-ATF4 pathway was activated by vDSG2 and might contribute to the increased expression of TGF-β1 in cardiomyocytes.

In order to investigate the cause-and-effect relationship between ATF4 and TGF-β1, we overexpressed ATF4 in cardiomyocytes and found that ATF4 overexpression increased TGF-β1 levels in HL-1 cells and NMVM (Fig. 6e, f). ATF4 knockdown via CRISPR-Cas9 did not significantly change TGF-β1 in HL-1 (Additional file 1: Fig. S11c, d). However, ATF4 knockdown attenuated BFA-induced expression of TGF-β1 in HL-1 cells (Additional file 1: Fig. S11e). In parallel, the levels of TGF-β1 were decreased significantly after ATF4 knockdown in HL-vDSG2 cells (Fig. 6g). Knockdown of ATF4 was also performed in NMVM from *Dsg2*$^{F536C/F536C}$ mice via adenovirus, and the results validated that ATF4 knockdown ameliorated the enhanced expression of TGF-β1 in cardiomyocytes (Fig. 6h). Furthermore, GSK2606414, an inhibitor of p-PERK [39], attenuated the increased expression of ATF 4 and TGF-β1 in HL-vDSG2 cells

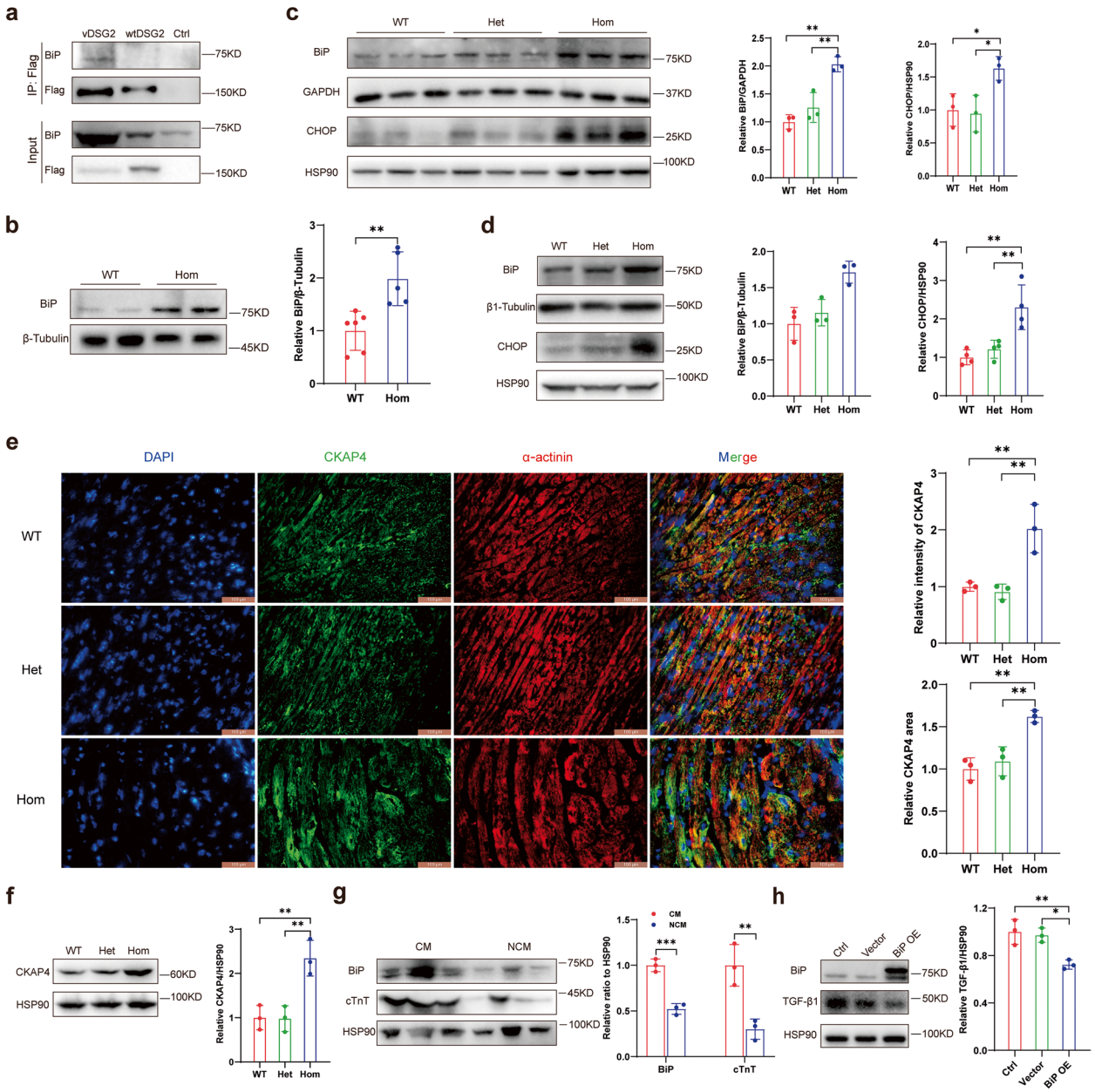

Fig. 5 DSG2-F536C promoted the expression of TGF-β1 via inducing endoplasmic reticulum stress in cardiomyocytes. **a** Co-IP demonstrated that BiP could interact with vDSG2 in HL-1 cells. **b** Representative western blot and quantification of BiP protein levels in NMVM from *Dsg2*$^{F536C/F536C}$ (Hom) and WT mice. $N=6$ in WT group, $N=5$ in Hom group. **c** Representative western blot and quantification of BiP and CHOP levels in hearts from 10-week-old *Dsg2*$^{WT/WT}$(WT), *Dsg2*$^{F536C/WT}$ (Het) and *Dsg2*$^{F536C/F536C}$ (Hom) mice. $N=3$ in each group. **d** Representative western blot and quantification of BiP and CHOP protein levels in the hearts from1-week-old WT, Het and Hom mice. $N=3$ or 4 in each group. **e** Representative immunofluorescence and quantification of CKAP4 intensity and area in hearts from 10-week-old WT, Het and Hom mice. $N=3$ in each group. **f** Representative western blot and quantification of CKAP4 protein levels in hearts from 10-week-old WT, Het and Hom mice. **g** Representative western blot and quantification of BiP and cTnT protein levels in adult mouse cardiomyocytes (CM) and non-cardiomyocytes (NCM) from 10-week-old *Dsg2*$^{F536C/F536C}$ mice. **h** Representative western blot and quantification of TGF-β1 protein levels in HL- vDSG2 cells with overexpression of BiP. $N=3$ in each group. Kruskal–Wallis test with Dunn's multiple comparison test was used to analyze the relative ratio of BiP/β-Tubulin in panel d. Otherwise, ordinary one-way ANOVA with Turkey's multiple comparisons test or Unpaired t-test was used to analyze the data, * $p<0.05$, **: $p<0.01$, ***: $p<0.001$

in a dose-dependent manner (Fig. 6i, Additional file 1: Fig. S11f), which was further validated in AMVM and NMVM from $Dsg2^{F536C/F536C}$ mice (Fig. 6j). Together, these results demonstrated that DSG2-F536C promoted the expression of TGF-β1 via PERK-ATF4 signaling in cardiomyocytes.

The p-PERK inhibitor ameliorated cardiac fibrosis and cardiac systolic dysfunction in $Dsg2^{F536C/F536C}$ mice

The p-PERK inhibitor GSK2606414 showed profound effects on the alleviation of increased TGF-β1 expression induced by DSG2-F536C in cardiomyocytes, prompting us to investigate its effects on cardiac fibrosis and cardiac systolic dysfunction in $Dsg2^{F536C/F536C}$ mice. Four-to five-week-old $Dsg2^{F536C/F536C}$ mice were randomly treated with DMSO (control group) or GSK2606414 (GSK group, Fig. 7a). After 4 weeks of treatment, GSK2606414 retarded progressive cardiac enlargement, thinning of the ventricular wall, and cardiac systolic dysfunction in $Dsg2^{F536C/F536C}$ mice compared with DMSO (Fig. 7b, c). Masson's staining demonstrated that the administration of GSK2606414 significantly reduced cardiac fibrosis and improved the thickness of the left ventricular free wall (Fig. 7d, e). Immunoblotting verified that GSK2606414 treatment decreased ATF4, TGF-β1 levels and p-SMAD2/SMAD2 ratio in the hearts of $Dsg2^{F536C/F536C}$ mice (Fig. 7f, g). All these results indicated ATF4/TGF-β1 signaling played an important role in ACM caused by $Dsg2^{F536C}$ variant, and inhibition of ATF4/TGF-β signaling could attenuate the progressive cardiac fibrosis and systolic dysfunction in $Dsg2^{F536C/F536C}$ mice.

Discussion

In this study, we identified the $DSG2^{F531C}$ variant in patients with ACM from a large family that were all homozygous carriers of the $DSG2^{F531C}$ variant. To elucidate the pathogenic role of this variant, we generated $Dsg2^{F536C}$ knock-in mice and found homozygous mice presenting typical characteristics of ACM, including cardiac enlargement, cardiac systolic dysfunction, and cardiac fibrosis in both ventricles. However, these features were absent in mice with the heterozygous $Dsg2^{F536C}$ variant, even under chronic pharmacological stress with ISO. Mechanistic investigations demonstrated that DSG2-F536C was misfolded, recognized by the chaperone BiP in ER, and was degraded via the UPS. Meanwhile, the variant protein induced ER stress, activated PERK-ATF4 signaling, and subsequently enhanced the expression of TGF-β1 in cardiomyocytes, which activated cardiac fibroblasts in a paracrine manner and promoted cardiac fibrosis in ACM. Inhibition of the PERK-ATF4 pathway attenuated the increased TGF-β1 expression, progressive cardiac fibrosis, and systolic dysfunction in $Dsg2^{F536C/F536C}$ ACM mice (Fig. 8).

Although previous studies have identified homozygous $DSG2^{F531C}$ variant in ACM patients, its pathogenicity and genetic mode of inheritance remain uncertain [16–19]. This study identified $DSG2^{F531C}$ variant in a large family with 8 ACM patients. The pedigree investigation revealed that the $DSG2^{F531C}$ variant might contribute to ACM through an autosomal recessive inheritance pattern, distinguishing it from the majority of pathogenic variations in desmosomal genes [40]. Accordingly, in $Dsg2^{F536C}$ knock-in mice, we observed that only mice harboring homozygous variants presented a severe and fully penetrant ACM phenotype, whereas $Dsg2^{F536C/WT}$ mice presented no abnormalities in cardiac structure, systolic function, histology, or molecular signature. Competitive and high-intensity endurance exercise could increase the likelihood of developing ACM in heterozygous desmosomal variant carriers, mainly because of the high activity of the sympathetic nervous system during exercise [41, 42], which could be simulated by pharmacological stress with chronic infusion of ISO [29]. In this study, there were no differences in cardiac geometry, function, or histological findings between

(See figure on next page.)

Fig. 6 DSG2-F536C induced the expression of TGF-β1 via PERK-ATF4 signaling pathway. **a** Schematic showing the three UPR pathways in mammals. Created with Biorender.com under academic license. **b** Representative western blot and quantification of ATF4 protein levels in HI-1 cells (Ctrl), HL-1 cells with stable expression of vDSG2 (vDSG2), and HL-1 cells with stable expression of wtDSG2 (wtDSG2). $N = 3$ in each group. **c** Representative western blot and quantification of p-PERK/PERK ratio, and p-eIF2α/eIF2α ratio in HI-1 cells (Ctrl), HL-vDSG2 (vDSG2), and HL-wtDSG2 (wtDSG2). $N = 3$ in each group. **d** Representative western blot and quantification of the levels of ATF4, p-PERK/PERK ratio, and p-eIF2α/eIF2α ratio in hearts from 10-week-old $Dsg2^{WT/WT}$ (WT), $Dsg2^{F536C/WT}$ (Het) and $Dsg2^{F536C/F536C}$ (Hom) mice. $N = 4$ in each group. **e** Representative western blot and quantification of the levels of TGF-β1 protein levels in HL-1 cells with overexpression of ATF4 via lentivirus. $N = 3$ in each group. **f** Representative western blot and quantification of the levels of TGF-β1 protein levels in NMVM with overexpression of ATF4 via adenovirus. $N = 3$ in each group. **g** Representative western blot and quantification of the levels of TGF-β1 protein levels in HL-vDSG2 cells with ATF4 KD. $N = 3$ in each group. **h** Representative western blot and quantification of the levels of TGF-β1 protein levels in NMVM with ATF4 KD. NMVM were isolated from $Dsg2^{F536C/F536C}$ mice. $N = 3$ in each group. **i** Representative western blot and quantification of the levels of TGF-β1 protein levels in HL-vDSG2 treated with GSK2606414 (0.4 μM for 24 h). $N = 3$ in each group. **j** Representative western blot and quantification of the levels of TGF-β1 protein levels in AMVM and NMVM treated with GSK2606414 (0.2 μM for 24 h). AMVM and NMVM were isolated from $Dsg2^{F536C/F536C}$ mice. $N = 3$ in each group. Ordinary one-way ANOVA with Turkey's multiple comparisons test was used to analyze the data, * $p < 0.05$, **: $p < 0.01$, ***: $p < 0.001$

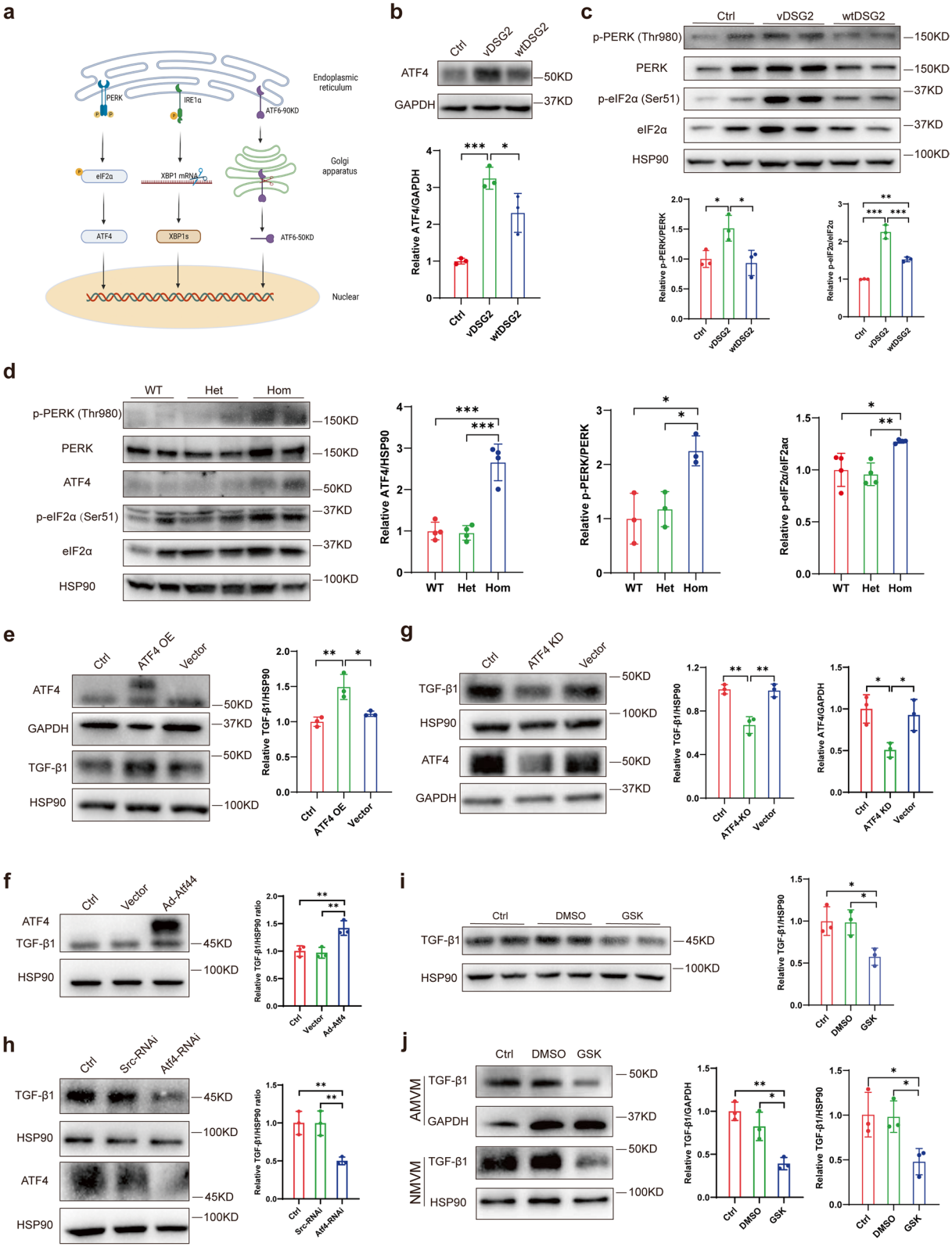

Fig. 6 (See legend on previous page.)

$Dsg2^{F536C/WT}$ and $Dsg2^{WT/WT}$ mice after 2-week ISO administration. Accordingly, $Dsg2^{F536C}$ variant may be associated with autosomal recessive inherited ACM. This finding is of great significance for the management of family members who are heterozygous $DSG2^{F531C}$ variant carriers. Family members with pathogenic gene variants but without phenotypes are recommended to avoid competitive or high-intensity endurance exercise [20]. In this study, $Dsg2^{F536C/F536C}$ mice presented no features of ACM after chronic and high-intensity pharmacological stress, indicating that exercise recommendations might be provided on an individual basis to some pathogenic gene carriers.

Activation of quiescent fibroblasts by TGF-β1 and subsequent remodeling of extracellular matrix proteins are key pathophysiological processes of cardiac fibrosis [33]. A previous study demonstrated $Dsg2^{W2A}$ pathogenic variant could activate and release TGF-β1 through integrin-αV/β6 pathway, leading to cardiac fibrosis and ACM [12]. The present study not only identified the activation of TGF-β1 signaling but also revealed that the $Dsg2^{F536C}$ variant could directly promoted the expression of TGF-β1 in cardiomyocytes. The increased TGF-β1 activated the canonical TGF-β1 pathway in fibroblasts by increasing the phosphorylation of SMAD2/3, which was transferred into the nucleus, promoted the expression of extracellular matrix-related genes, and led to cardiac fibrosis [43]. Moreover, we identified that elevated TGF-β1 from cardiomyocytes harboring homozygous $Dsg2^{F536C}$ variant was one of the primary causes of cardiac fibrosis in ACM. Interestingly, cardiac fibroblasts from $Dsg2^{F536C/F536C}$ mice exhibited similar TGF-β1 levels to those from WT mice. This suggested that cardiac fibroblasts were passively activated by TGF-β1 secreted from adjacent cardiomyocytes in $Dsg2^{F536C/F536C}$ mice. Previous studies demonstrated that the loss of plakophilin-2 and the mutation of transmembrane protein 43 enhanced the expression of TGF-β1 in cardiomyocytes in ACM [44, 45]. However, the mechanism underlying the increased expression of TGF-β1 caused by desmosomal gene variants is unclear.

A previous study showed the presence of ER stress in the hearts of ACM mice, yet the mechanisms underlying ERS and its significance in ACM remain unclear [46]. In this study, it was found that DSG2-F536C was misfolded and interacted with BiP in the ER. The interaction of DSG2-F536C and BiP could release the three stress sensors, PERK, ATF6, and IRE1 at the ER membrane, which would activate the 3 corresponding downstream signaling and induce ER stress. The elevated levels of BiP, CHOP, and ER expansion in cardiomyocytes verified ER stress in the hearts of $Dsg2^{F536C/F536C}$ mice. Further investigation revealed that ER stress upregulated the expression of TGF-β1 in cardiomyocytes, consequently promoting cardiac fibrosis in $Dsg2^{F536C/F536C}$ mice. The correlation between ER stress and increased TGF-β1 levels was shown in Crohn's disease [47]. However, it remains unclear how ER stress leads to the elevated levels of TGF-β1. Increased ATF4 levels with unchanged levels of ATF6 and XBP1s in cardiac tissues from $Dsg2^{F536C/F536C}$ mice and HL-vDSG2 cells indicated that only the PERK-ATF4 pathway was selectively activated in cardiomyocytes harboring the homozygous $Dsg2^{F536C}$ variant. This may be related to chronic ER stress induced by the continuous expression of the vDSG2. A previous study showed that activities of IRE1α—XBP1s and the ATF6 pathway were attenuated while the PERK-ATF4 pathway remained active during chronic ER stress [48], which might be related to the inhibition of global protein translation [49].

After disassociation from BiP in the ER lumen, PERK normally form homodimers and undergo autophosphorylation. This is followed by the phosphorylation of eIF2α. Phosphorylated eIF2α functions to inhibit the translation of cap-dependent mRNA, while promoting the translation of a subset of mRNA with small upstream open reading frames, including ATF4 [50, 51]. As a transcription factor, ATF4 binds to the target gene promoters, thereby facilitating the transcription of genes involved in apoptosis, redox regulation, and amino acid metabolism [52, 53]. Studies have reported conflicting results on the role of ATF4 in the heart. Some

(See figure on next page.)

Fig. 7 Inhibition of ATF4/TGF-β1 signaling ameliorated cardiac dysfunction and cardiac fibrosis in $Dsg2^{F536C/F536C}$ mice. **a** Schematic diagram showing the treatment strategy with GSK2606414 in $Dsg2^{F536C/F536C}$ mice. Created with Biorender.com under academic license. **b** Representative images of M-mode echocardiography of LV geometry and systolic function in $Dsg2^{F536C/F536C}$ mice at baseline and after 4-week treatment with GSK2606414 or DMSO. **c** Quantification of LV geometry (LVDD and LVDS) and systolic function (LVEF and LVFS) in $Dsg2^{F536C/F536C}$ mice at baseline and after 4-week treatment with GSK2606414 or DMSO. $N=4$ in control group and $N=9$ in GSK2606414 group. **d** Representative images of Masson's staining in $Dsg2^{F536C/F536C}$ mice after 4-week treatment with GSK2606414 or DMSO. Scale bar 1 mm. **e** Quantification of global fibrosis and wall thickness of both ventricles in $Dsg2^{F536C/F536C}$ mice after 4-week treatment with GSK2606414 or DMSO. $N=5$ in GSK group, and $N=3$ in control group. **f-g** Representative western blot (**f**) and quantification (**g**) of TGF-β1, ATF4 protein levels and p-SMAD2/SMAD2 ratio in hearts from $Dsg2^{F536C/F536C}$ mice after 4-week treatment with GSK2606414 or DMSO. $N=4$ in GSK group, and $N=3$ in control group. Unpaired t-test were used to analyze the data, * $p<0.05$, **: $p<0.01$, ***: $p<0.001$, ns, not significant

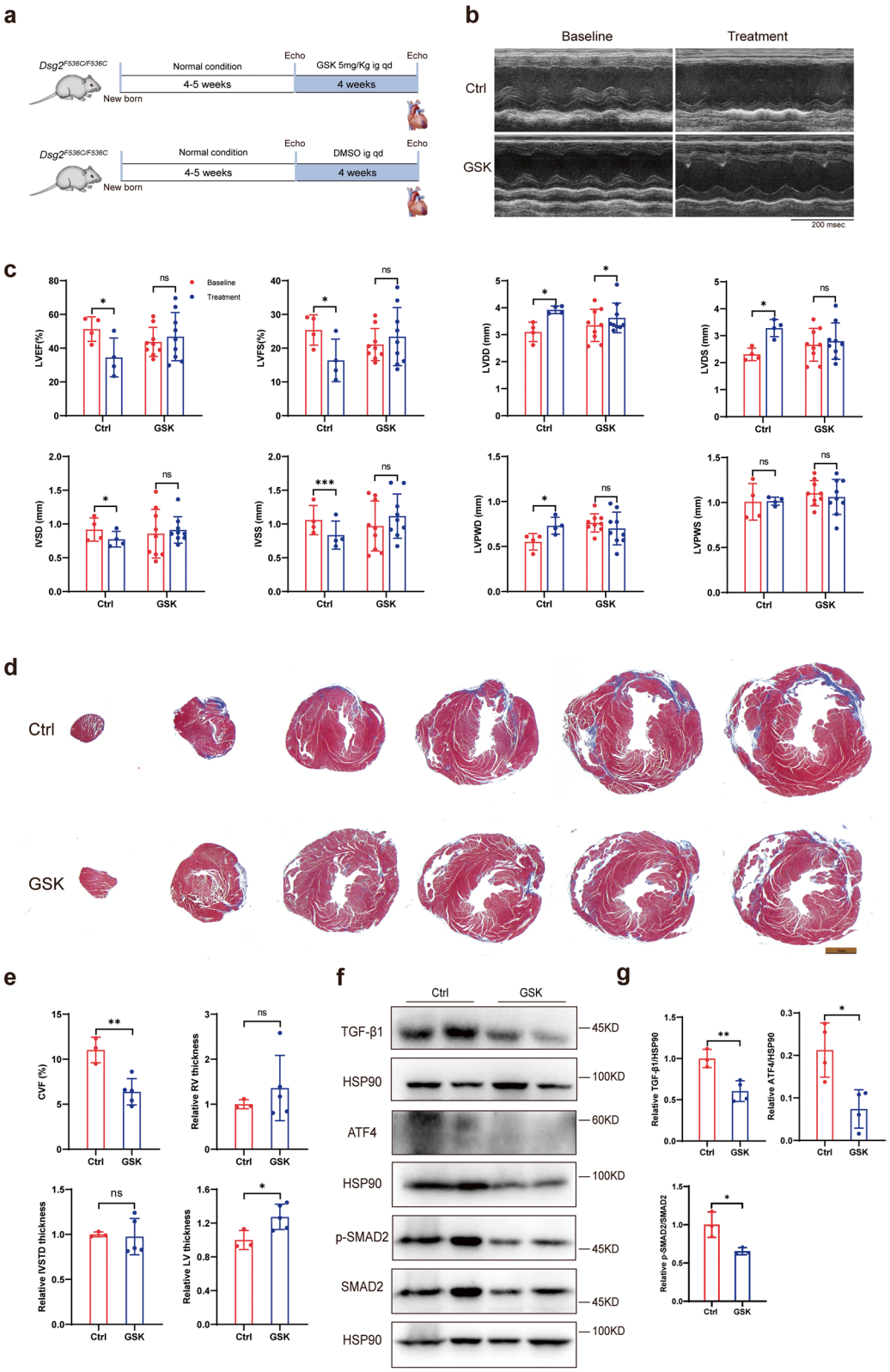

Fig. 7 (See legend on previous page.)

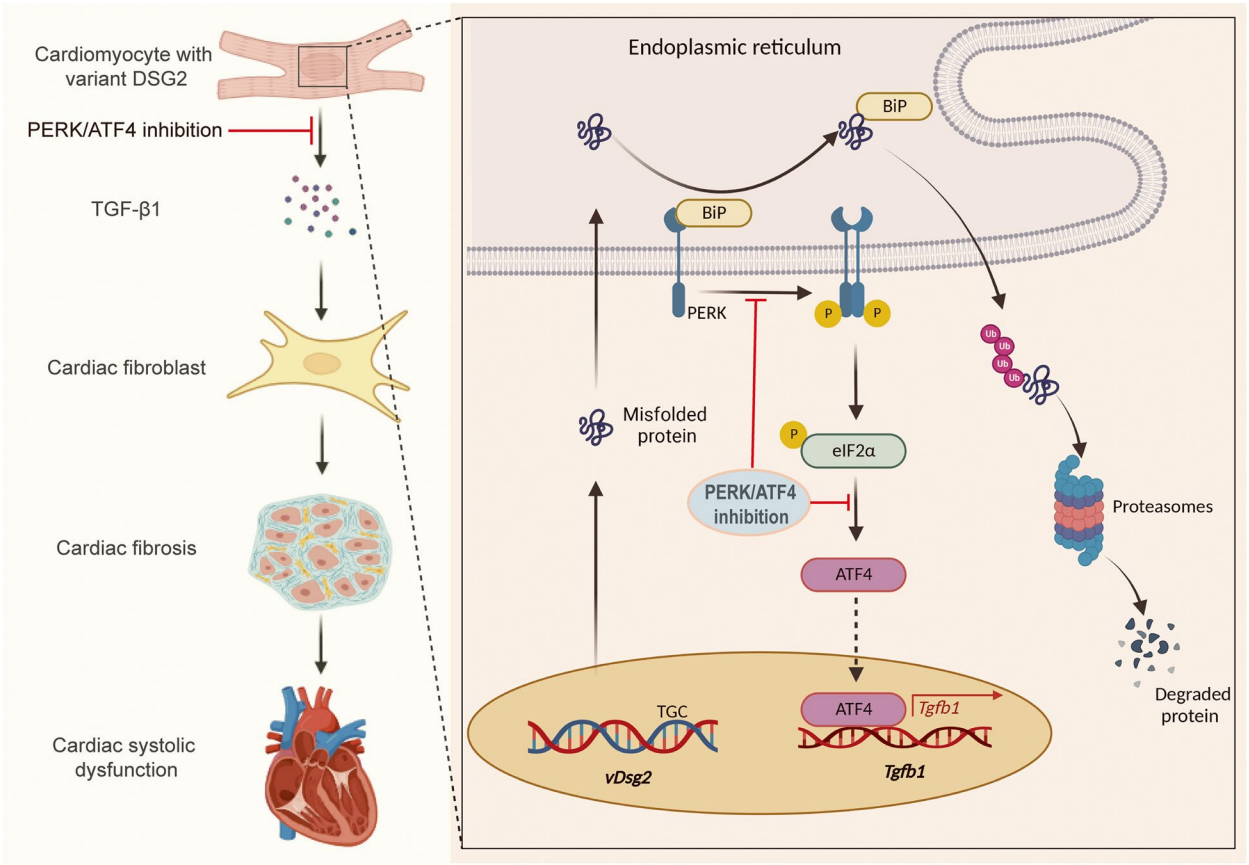

Fig. 8 Schematic conclusion of the main findings of the study. *Dsg2*^{F536C} in the cardiomyocyte leads to the misfolding of the variant protein, which is recognized by the chaperon BiP in the ER, followed by translocating to cytosol to be degraded via ubiquitin–proteasome pathway. Meanwhile, the variant protein activated the PERK-ATF4 signaling pathway, and subsequently increase the expression of TGF-β1 in cardiomyocytes, which promotes cardiac fibrosis and heart failure in ACM via activating cardiac fibroblasts. Notably, inhibition of the PERK/ATF4 signaling could attenuate the increased TGF-β1 levels and cardiac fibrosis in ACM mice. Created with Biorender.com under academic license

researchers have found that ATF4 had cardioprotective effects under hemodynamic and mitochondrial stress via its antioxidant effects [54, 55]. However, ATF4 overexpression in cardiomyocytes induced lethal cardiac atrophy by enhancing autophagy [56]. Another study found that increased ATF4 levels mediated the impaired cardiomyocyte maturation induced by the RYR2 variant [57]. Our study showed that ATF4 accelerated cardiac fibrosis by increasing TGF-β1 levels in cardiomyocytes. In addition, the expression of TGF-β1 in cardiomyocytes could be reversed by a p-PERK inhibitor or ATF4 knockdown, indicating that the activation of PERK/ATF4 signaling was a novel mechanism underlying the elevated TGF-β1 levels in ACM. In vivo experiments validated the beneficial effects of a p-PERK inhibitor in attenuating progressive cardiac fibrosis and cardiac systolic dysfunction in *Dsg2*$^{F536C/F536C}$ mice.

In addition to UPR, The ER associated degradation is the main protein degradation systems to deal with misfolded proteins in ER to attenuate the ER stress. Most of the misfolded proteins in ER are translocated to cytosol, where they are targeted with ubiquitin label by ubiquitin cascade reaction, and followed by the degradation in the proteasome [58]. Increased levels of vDSG2-Flag following MG132 treatment, along with elevated ubiquitination levels of vDSG2 in HL-V cells, indicate that vDSG2 may be degraded through the ER-associated degradation pathway. Targeting the ubiquitination and degradation of proteins has emerged as a new therapeutic strategy [59]. Mass spectrometry analysis identified TRIM21 and USP10 as potential candidates interacting with vDSG2. TRIM21 is an intracellular ubiquitin ligase [60], whereas USP10 functions as a deubiquitinating enzyme [61]. These findings suggest that TRIM21 and

USP10 may play roles in the ubiquitination and degradation of DSG2, highlighting their potential as therapeutic targets for DSG2-related ACM in the future.

Conclusions

Hyperactivation of the ATF4/TGF-β1 signaling in cardiomyocytes is a novel driver of progressive cardiac fibrosis in ACM. The identification of these mechanisms provides potential therapeutic targets for ACM management.

Abbreviations

ACM	Arrhythmogenic cardiomyopathy
AMVM	Adult mouse ventriclar myocytes
ATF4	Activating transcription factor 4
ATF6	Activating transcription factor 6
BFA	Brefeldin A
BiP	Immunoglobulin heavy chain binding protein
BSA	Bovine serum albumin
CHOP	C/EBP-homologous protein
CKAP4	Cytoskeleton associated protein 4
CVF	Collagen volume fraction
CQ	Chloroquine
DEGs	Differentially expressed genes
DMEM	Dulbecco's modified Eagle's medium
DSG2	Desmoglein-2
DSP	Desmoplakin
ECG	Electrocardiography
eIF2α	Eukaryotic translation initiation factor 2α
ESC	Embryonic stem cell
FBS	Fetal bovine serum
GO	Gene ontology
GSEA	Gene set enrichment analysis
HSPA5	Heat shock protein family A member 5
IRE1	Inositol requiring enzyme 1
ISO	Isoproterenol
NMVM	Neonatal mouse ventricular myocytes
PERK	Protein kinase R like ER kinase
PFA	Paraformaldehyde
RMSD	Root Mean Square Deviation
TGF-β1	Transforming growth factor β1
UPR	Unfolded protein response
UPS	Ubiquitin-proteasome system
vDSG2	Variant DSG2
WT	Wild type
wtDSG2	Wild-type DSG2
XBP1s	Sliced X-box binding protein 1

Supplementary Information

The online version contains supplementary material available at https://doi.org/10.1186/s12916-024-03593-8.

Additional file 1: Figure S1. Representative ECG of persistent ventricular tachycardia in an ACM patient with *DSG2*^{F531C} variant. Figure S2. Comparation of amino acids sequence of DSG2 across the cadherin family number and between human and mouse. (a) The variant (F531C) was located in an evolutionary highly conservative area across the cadherin family proteins. (b) The Phe 536 of mouse DSG2 (black arrow) was homologue to the Phe 531 of human DSG2 (red arrow). Figure S3. Generation of *Dsg2*^{F536C} variant mice. (a) Generation of the variant allele. (b) Southern blot analysis on four initially screened neomycin-resistant embryonic stem (ES) clones. The left panel displayed HpaI digest (19.9 K and 10 K) and the right panel displayed NheI digest for Neo (14.2 K). Clone B6 served as the wild-type ES clone, while clones E11 and E1 were identified as correctly targeted clones. Clone B10, however, was determined to be an incorrectly targeted clone. (c) Sequencing result to showed correct change of TTC (encoding phenylalanine) to TGC (encoding cysteine). (d) Genotyping. The PCR products were 466 bp for Homozygous (*Dsg2*$^{F536C/F536C}$) and 368 bp for wild-type (*Dsg2*$^{WT/WT}$). Figure S4. Comparison of left ventricular free wall thickness among 10-week-old *Dsg2*$^{WT/WT}$ (WT), *Dsg2*$^{F536C/WT}$(Het), and *Dsg2*$^{F536C/F536C}$ (Hom) mice. Ordinary one-way ANOVA and Turkey's multiple comparisons test was used to analyze the data, ***: $p < 0.001$; ns, not significant. $N = 13$ in WT group, $N = 16$ in Het group, and $N = 19$ in Hom group. Figure S5. Homozygous *Dsg2*$^{F536C/F536C}$ mice showed significant biventricular fibrosis. (a) Representative images of Masson's staining in 4-week-old *Dsg2*$^{WT/WT}$ (WT), *Dsg2*$^{F536C/WT}$ (Het) and *Dsg2*$^{F536C/F536C}$ (Hom) mice. (b) Quantification of biventricular CVF, thickness of both free ventricular walls and interventricular septum in 4-week-old WT, Het and Hom mice. $N = 5$ in each group. ***: $p < 0.001$, **: $p < 0.01$, *: $p < 0.05$. (c) Quantification of interventricular septum thickness in *Dsg2*$^{F536C/F536C}$ mice from 2- to 10-week-old. $N = 5$ in each group. #: $p < 0.05$ compared with the heart of 4-week-old mice; ns, not significant. One-way ANOVA and Turkey's multiple comparisons test was used to analyze the data. Figure S6. Failed to induce the phenotypes of ACM under the chronical pharmacological stress with ISO in heterozygous *Dsg2*$^{F536C/WT}$ mice. (a) Schematic diagram showing the strategy of the chronically pharmacological stress with ISO. Created with Biorender.com under academic license. (b) Representative images of M-mode echocardiography of LV geometry and systolic function in WT and *Dsg2*$^{F536C/WT}$ (Het) mice after 2-week treatment with ISO. ns, not significant. (c) Quantification of LV geometry (LVDD, LVDS, thickness of free wall and interventricular septum) and systolic function (LVEF and LVFS) in WT and Het mice after 2-week treatment with ISO. $N = 6$ in WT group, and $N = 8$ in Het group. ns, not significant. (d) Representative images of Masson's staining in WT and Het mice after 2-week treatment with ISO. Scale bar 1 mm. (e) Quantification of global fibrosis and wall thickness of both ventricles in WT and Het mice after 2-week treatment with ISO. $N = 6$ in WT group, and $N = 8$ in Het group. ns, not significant. Unpaired t-test was used to analyze the data. Figure S7. DSG2-F536C was degraded via the ubiquitin–proteasome signaling. (a) Relative mRNA levels of *Dsg2* in the hearts of 10-week-old WT, Het and Hom mice. $N = 3$ in each group. (b) Representative western blot and quantification of DSG2-Flag in HER293T cells transfected with plasmids with mutant or WT mice *Dsg2* cDNA and a C-terminal 3xflag epitope. The DSG2-Flag was detected by anti-DSG2 and anti-Flag antibody respectively. $N = 3$ in each group. (c) The predicted 3D model of extracellular and transmembrane domains (55th—619th amino acid) of wild-type DSG2 protein (blue) and the variant DSG2-F536C protein (green) via AlphaFold2. The black dashed box indicated a similar secondary structure at the variant site, and the purple indicated the mutated amino acid. (d) Comparison of the three-dimensional structures between vDSG2 (green) and wtDSG2 (blue). The red segments indicate the regions of abnormal folding in vDSG2, whereas the yellow segments represent the corresponding normal structure in wtDSG2. (e) Relative mRNA levels of *Dsg2* in HL-1 cells, HL-1 cells with stable expression of variant DSG2 (vDSG2) and wild type DSG2 (wtDSG2). $N = 3$ in each group. (f) Representative western blot and quantification of DSG2-Flag and β-Catenin protein levels in HL-wtDSG2 treated with MG132. $N = 3$ in both groups. Kruskal–Wallis test with Dunn's multiple comparison test was used to analyze DSG2-Flag levels in panel f. Otherwise, One-way ANOVA and Turkey's multiple comparisons test or Unpaired t test was used to analyze the data. *: $p < 0.05$, **: $p < 0.01$, ***: $p < 0.001$, ns, not significant. Figure S8. Activation of TGF-β1 pathway in the hearts of 10-week-old *Dsg2*$^{F536C/F536C}$ mice. (a) Heatmap of differentially expressed genes (DEGs) in the hearts of 10-week-old *Dsg2*$^{WT/WT}$ (WT), *Dsg2*$^{F536C/WT}$ (Het) and *Dsg2*$^{F536C/F536C}$ (Hom) mice. $N = 4$ in each group. (b) Volcano plot and quantification of DEGs between different groups. $N = 4$ in each group. (c) Venn diagram between Hom vs Het and Hom vs WT mice. $N = 4$ in each group. (d) Gene Ontology (GO) analyses for upregulated genes in the hearts of 10-week-old Hom mice compared with both WT and Het mice. (e) Representative western blot and quantification of TGF-β1 protein levels in the hearts from 1-week-old WT, Het and Hom mice. $N = 3$ in each group. Kruskal–Wallis test with Dunn's multiple comparison test was used to analyze the data. Figure S9. Overexpression of DSG2-F536C in HL-1 cells significantly promoted fibroblast

activation via SMADs signaling. (a) UMAP map of snRNA-seq displaying 9 distinct cellular clusters. (b) Feature plot showing expression of *DSG2* among different cellular clusters. (c) Violin plot showing *DSG2* expression in human hearts. (d) Representative western blot and quantification of DSG2 levels in neonatal rat ventricular myocytes (NRVM) and neonatal rat fibroblasts (NRFB). $N=3$ in both groups. ***: $p<0.001$. (e) The conditioned medium from HL-vDSG2 cells promoted NMFB migration by wound healing assay compared with conditioned medium from HL-1 and HL-wtDSG2 cells. $N=3$ in each group. *: $p<0.05$ compared with HL-1, **: $p<0.01$ compared with HL-1 cells, #: $p<0.05$ compared with HL-wtDSG2 cells. (f) Representative western blot and quantification of α-SMA protein levels in NMFB treated with conditioned medium of HL-1, HL-vDSG2 and HL-wtDSG2 cells. $N=4$ in each group. *: $p<0.05$. (g-h) Representative western blot and quantification of p-SMAD2/SMAD2 ratio (g) and p-SMAD3/SMAD3 ratio (h) in NMFB treated with conditioned medium from HL-1, HL-vDSG2 and HL-wtDSG2 cells (red arrow indicates p-SMAD3). $N=4$ in each group. ***: $p<0.001$. Kruskal–Wallis test with Dunn's multiple comparison test was used to analyze p-SMAD3 in the panel h. Otherwise, One-way ANOVA and Turkey's multiple comparisons test or Unpaired t test was used to analyze the data. Figure S10. DSG2-F536C promoted the expression of TGF-β1 via inducing endoplasmic reticulum stress in cardiomyocytes. (a) Representative western blot and quantification of BiP protein levels in HL-1 cells, HL-1 cells with stable expression of variant DSG2 (vDSG2), and HL-1 cells with stable expression of wild type DSG2 (wtDSG2). $N=3$ in each group. (b) Representative western blot and quantification of TGF-β1 protein levels in HL-1 cells treated with placebo or brefeldin A (BFA, 2.5ug/L for 12 h). $N=3$ in each group. One-way ANOVA and Turkey's multiple comparisons test or unpaired t-test was used to analyze the data, **: $p<0.01$, ***: $p<0.001$. Figure S11. DSG2-F536C promoted the expression of TGF-β1 in cardiomyocytes via PERK-ATF4 pathway. (a) Representative western blot and quantification of XBP1s and ATF6-50KD in HL-1 (Ctrl), HL-vDSG2 and HL-wtDSG2 cells. $N=3$ in each group. (b) Representative western blot and quantification of ATF6-50KD, XBP1u and XBP1s in the hearts of 10-week-old $Dsg2^{WT/WT}$ (WT), $Dsg2^{F536C/WT}$ (Het) and $Dsg2^{F536C/F536C}$ (Hom) mice. $N=3$ in each group. (c) Representative western blot and quantification of ATF4 in HL-1 cells treated with CRISPR-Cas9 with sgRNA targeting ATF4. $N=3$ in each group. (d) Representative western blot and quantification of TGF-β1 in HL-1 cells with ATF4-KD. $N=3$ in each group. (e) Representative western blot and quantification of ATF4 and TGF-β1 protein levels in HL-1 cells with ATF4-KD under ER stress induced by BFA. $N=3$ in each group. (f) Representative western blot and quantification of ATF4 and TGF-β1 in HL-vDSG2 cells treated with different doses of GSK2606414. $N=3$ in each group. One-way ANOVA and Turkey's multiple comparisons test was used to analyze the data. *: $p<0.05$, **: $p<0.01$, ***: $p<0.001$. Table S3. Lists of primary antibodies used in this study. Table S4. Primary sequence for genotyping. Table S5. Primary sequence for real time quantitative PCR. Table S6. Target for RNAi.

Additional file 2: Table S1. Clinical characterization of DSG2-F531C mutation-positive family members.

Additional file 3: Table S2. Results of mass spectrometry analysis of purified protein by immunoprecipitation with anti-Flag antibody in cultured cardiomyocytes with stable expression vDSG2.

Additional file 4. GSEA of DEGs between $Dsg2^{F536C/F536C}$ and $Dsg2^{F536C/WT}$ or $Dsg2^{WT/WT}$ mice.

Additional file 5. Uncut blot

Additional file 6. ARRIVE guidelines checklist.

Acknowledgements
Not applicable.

Authors' contributions
Conceptualization: BZ, YX and BY. Methodology: BZ, YW, CS and CZ. Investigation: BZ, YW, CZ and JX1; Software: YZ, JX2, and XY. Writing – Original Draft: BZ and YW. Writing – Review & Editing: CS, BZ, DWW, YX and BY. Resources: BY, DWW, and XZ. Funding acquisition: XZ, and BY. Supervision: YX and BY. All authors read and approved the final manuscript.

Funding
This work was supported by grants from the Top-level Clinical Discipline Project of Shanghai Pudong District Grant/Award (PWYgf2021-01), The health science and technology project of Shanghai Pudong (PW2023A-17), the Science and Technology Plan Project of Health Commission of Jiangxi Province (202312389), National Natural Science Foundation of China (No. 81070158 to BY, No. 82370323 to BY, No. 81170161 to XZ), Health Commission of Shanghai Pudong District, China (PW2019D-1), and Shanghai Committee of Science and Technology, China (19DZ1930402).

Availability of data and materials
The datasets used and/or analyzed during the current study are available from the corresponding author on reasonable request.

Declarations

Ethics approval and consent to participate
This study was approved by the Ethics Committee of the First Affiliated Hospital of Nanjing Medical University (NO.2011-SR-014) and the informed consent was obtained from all the participants before undergoing evaluation and testing. Animal experiments were approved by the Institutional Animal Care and Use Committee of Nanjing Medical University (approval number: IACUC-14030160).

Consent for publication
Not applicable.

Competing interests
The authors declare no competing interests.

Author details
[1]Department of Cardiology, Shanghai East Hospital, Tongji University School of Medicine, 150 Jimo Road, Pudong, Shanghai 200120, P.R. China. [2]Department of Cardiology, the First Affiliated Hospital of Nanjing Medical University, 300 Guangzhou Road, Nanjing 210029, P.R. China. [3]Shanghai East Hospital, School of Life Sciences and Technology, Tongji University, 150 Jimo Road, Pudong, Shanghai 200120, P.R. China. [4]State Key Laboratory of Reproductive Medicine, the Centre for Clinical Reproductive Medicine, Department of Cardiology, the First Affiliated Hospital of Nanjing Medical University, 300 Guangzhou Road, Nanjing 210029, P.R. China. [5]Model Animal Research Center, Nanjing University, Nanjing, China.

Received: 18 March 2024 Accepted: 27 August 2024
Published online: 04 September 2024

References

1. Corrado D, Link MS, Calkins H. Arrhythmogenic right ventricular cardiomyopathy. N Engl J Med. 2017;376:61–72.
2. van der Voorn SM, Te Riele A, Basso C, Calkins H, Remme CA, van Veen TAB. Arrhythmogenic cardiomyopathy: pathogenesis, pro-arrhythmic remodelling, and novel approaches for risk stratification and therapy. Cardiovasc Res. 2020;116:1571–84.
3. Corrado D, Basso C, Judge DP. Arrhythmogenic Cardiomyopathy. Circ Res. 2017;121:784–802.
4. Vermij SH, Abriel H, van Veen TA. Refining the molecular organization of the cardiac intercalated disc. Cardiovasc Res. 2017;113:259–75.
5. Pilichou K, Nava A, Basso C, Beffagna G, Bauce B, Lorenzon A, et al. Mutations in desmoglein-2 gene are associated with arrhythmogenic right ventricular cardiomyopathy. Circulation. 2006;113:1171–9.
6. Gandjbakhch E, Redheuil A, Pousset F, Charron P, Frank R. Clinical Diagnosis, Imaging, and Genetics of Arrhythmogenic Right Ventricular Cardiomyopathy/Dysplasia: JACC State-of-the-Art Review. J Am Coll Cardiol. 2018;72:784–804.
7. Hermida A, Fressart V, Hidden-Lucet F, Donal E, Probst V, Deharo JC, et al. High risk of heart failure associated with desmoglein-2 mutations compared to plakophilin-2 mutations in arrhythmogenic right ventricular cardiomyopathy/dysplasia. Eur J Heart Fail. 2019;21:792–800.
8. Austin KM, Trembley MA, Chandler SF, Sanders SP, Saffitz JE, Abrams DJ, et al. Molecular mechanisms of arrhythmogenic cardiomyopathy. Nat Rev Cardiol. 2019;16:519–37.

9. Garcia-Gras E, Lombardi R, Giocondo MJ, Willerson JT, Schneider MD, Khoury DS, et al. Suppression of canonical Wnt/beta-catenin signaling by nuclear plakoglobin recapitulates phenotype of arrhythmogenic right ventricular cardiomyopathy. J Clin Invest. 2006;116:2012–21.
10. Asatryan B, Asimaki A, Landstrom AP, Khanji MY, Odening KE, Cooper LT, et al. Inflammation and Immune Response in Arrhythmogenic Cardiomyopathy: State-of-the-Art Review. Circulation. 2021;144:1646–55.
11. Caforio ALP, Re F, Avella A, Marcolongo R, Baratta P, Seguso M, et al. Evidence from family studies for autoimmunity in Arrhythmogenic right ventricular cardiomyopathy: associations of circulating anti-heart and anti-intercalated disk autoantibodies with disease severity and family history. Circulation. 2020;141:1238–48.
12. Schinner C, Xu L, Franz H, Zimmermann A, Wanuske MT, Rathod M, et al. Integrin-αVβ6. Circulation. 2022;146:1610–26.
13. Zhang B, Wu Y, Yang X, Xiang Y, Yang B. Molecular insight into arrhythmogenic cardiomyopathy caused by DSG2 mutations. Biomed Pharmacother. 2023;167:115448.
14. Wiseman RL, Mesgarzadeh JS, Hendershot LM. Reshaping endoplasmic reticulum quality control through the unfolded protein response. Mol Cell. 2022;82:1477–91.
15. van Anken E, Bakunts A, Hu CA, Janssens S, Sitia R. Molecular evaluation of endoplasmic reticulum homeostasis meets humoral immunity. Trends Cell Biol. 2021;31:529–41.
16. Zhou X, Chen M, Song H, Wang B, Chen H, Wang J, et al. Comprehensive analysis of desmosomal gene mutations in Han Chinese patients with arrhythmogenic right ventricular cardiomyopathy. Eur J Med Genet. 2015;58:258–65.
17. Lin Y, Zhang Q, Zhong ZA, Xu Z, He S, Rao F, et al. Whole genome sequence identified a rare homozygous pathogenic mutation of the DSG2 gene in a familial Arrhythmogenic cardiomyopathy involving both ventricles. Cardiology. 2017;138:41–54.
18. Chen L, Rao M, Chen X, Chen K, Ren J, Zhang N, et al. A founder homozygous DSG2 variant in East Asia results in ARVC with full penetrance and heart failure phenotype. Int J Cardiol. 2019;274:263–70.
19. Murakami H, Tanimoto Y, Tanimoto K, Inoue S, Ishikawa T, Makita N, et al. Arrhythmogenic right ventricular cardiomyopathy in a Japanese patient with a homozygous founder variant of DSG2 in the East Asian population. Hum Genome Var. 2022;9:28.
20. Towbin JA, McKenna WJ, Abrams DJ, Ackerman MJ, Calkins H, Darrieux FCC, et al. 2019 HRS expert consensus statement on evaluation, risk stratification, and management of arrhythmogenic cardiomyopathy. Heart Rhythm. 2019;16:e301–72.
21. Corrado D, Perazzolo Marra M, Zorzi A, Beffagna G, Cipriani A, Lazzari M, et al. Diagnosis of arrhythmogenic cardiomyopathy: the Padua criteria. Int J Cardiol. 2020;319:106–14.
22. Tschopp O, Yang ZZ, Brodbeck D, Dummler BA, Hemmings-Mieszczak M, Watanabe T, et al. Essential role of protein kinase B gamma (PKB gamma/Akt3) in postnatal brain development but not in glucose homeostasis. Development. 2005;132:2943–54.
23. Huang K, Gao J, Du J, Ma N, Zhu Y, Wu P, et al. Generation and Analysis of GATA2(w/eGFP) Human ESCs Reveal ITGB3/CD61 as a Reliable Marker for Defining Hemogenic Endothelial Cells during Hematopoiesis. Stem Cell Reports. 2016;7:854–68.
24. Schrickel JW, Bielik H, Yang A, Schimpf R, Shlevkov N, Burkhardt D, et al. Induction of atrial fibrillation in mice by rapid transesophageal atrial pacing. Basic Res Cardiol. 2002;97:452–60.
25. Jiang K, Tu Z, Chen K, Xu Y, Chen F, Xu S, et al. Gasdermin D inhibition confers antineutrophil-mediated cardioprotection in acute myocardial infarction. J Clin Invest. 2022;132:e151268.
26. Ackers-Johnson M, Li PY, Holmes AP, O'Brien SM, Pavlovic D, Foo RS. A Simplified, Langendorff-Free Method for Concomitant Isolation of Viable Cardiac Myocytes and Nonmyocytes From the Adult Mouse Heart. Circ Res. 2016;119:909–20.
27 Reichart D, Lindberg EL, Maatz H, Miranda AMA, Viveiros A, Shvetsov N, et al. Pathogenic variants damage cell composition and single cell transcription in cardiomyopathies. Science. 2022;377:eabo1984.
28. Hoorntje ET, Te Rijdt WP, James CA, Pilichou K, Basso C, Judge DP, et al. Arrhythmogenic cardiomyopathy: pathology, genetics, and concepts in pathogenesis. Cardiovasc Res. 2017;113:1521–31.
29. Perez-Hernandez M, van Opbergen CJM, Bagwan N, Vissing CR, Marron-Linares GM, Zhang M, et al. Loss of nuclear envelope integrity and increased oxidant production cause DNA Damage in Adult Hearts Deficient in PKP2: a molecular substrate of ARVC. Circulation. 2022;146:851–67.
30. Wang P, Xu S, Xu J, Xin Y, Lu Y, Zhang H, et al. Elevated MCU expression by CaMKIIdeltaB limits pathological cardiac remodeling. Circulation. 2022;145:1067–83.
31. Jumper J, Evans R, Pritzel A, Green T, Figurnov M, Ronneberger O, et al. Highly accurate protein structure prediction with AlphaFold. Nature. 2021;596:583–9.
32. Henning RH, Brundel B. Proteostasis in cardiac health and disease. Nat Rev Cardiol. 2017;14:637–53.
33. Frangogiannis NG. Cardiac fibrosis. Cardiovasc Res. 2021;117:1450–88.
34. Gibb AA, Lazaropoulos MP, Elrod JW. Myofibroblasts and Fibrosis: Mitochondrial and Metabolic Control of Cellular Differentiation. Circ Res. 2020;127:427–47.
35. Khaminets A, Heinrich T, Mari M, Grumati P, Huebner AK, Akutsu M, et al. Regulation of endoplasmic reticulum turnover by selective autophagy. Nature. 2015;522:354–8.
36. Gubas A, Dikic I. ER remodeling via ER-phagy. Mol Cell. 2022;82:1492–500.
37. Bi X, Zhang G, Wang X, Nguyen C, May HI, Li X, et al. Endoplasmic Reticulum Chaperone GRP78 Protects Heart From Ischemia/Reperfusion Injury Through Akt Activation. Circ Res. 2018;122:1545–54.
38. Walter P, Ron D. The unfolded protein response: from stress pathway to homeostatic regulation. Science. 2011;334:1081–6.
39. Marciniak SJ, Chambers JE, Ron D. Pharmacological targeting of endoplasmic reticulum stress in disease. Nat Rev Drug Discov. 2022;21:115–40.
40. James CA, Syrris P, van Tintelen JP, Calkins H. The role of genetics in cardiovascular disease: arrhythmogenic cardiomyopathy. Eur Heart J. 2020;41:1393–400.
41. Gasperetti A, James CA, Cerrone M, Delmar M, Calkins H, Duru F. Arrhythmogenic right ventricular cardiomyopathy and sports activity: from molecular pathways in diseased hearts to new insights into the athletic heart mimicry. Eur Heart J. 2021;42:1231–43.
42. James CA, Bhonsale A, Tichnell C, Murray B, Russell SD, Tandri H, et al. Exercise increases age-related penetrance and arrhythmic risk in arrhythmogenic right ventricular dysplasia/cardiomyopathy-associated desmosomal mutation carriers. J Am Coll Cardiol. 2013;62:1290–7.
43. Frangogiannis NG. Transforming growth factor-beta in myocardial disease. Nat Rev Cardiol. 2022;19:435–55.
44. Dubash AD, Kam CY, Aguado BA, Patel DM, Delmar M, Shea LD, et al. Plakophilin-2 loss promotes TGF-beta1/p38 MAPK-dependent fibrotic gene expression in cardiomyocytes. J Cell Biol. 2016;212:425–38.
45. Zheng G, Jiang C, Li Y, Yang D, Ma Y, Zhang B, et al. TMEM43-S358L mutation enhances NF-κB-TGFβ signal cascade in arrhythmogenic right ventricular dysplasia/cardiomyopathy. Protein Cell. 2019;10:104–19.
46. Pitsch M, Kant S, Mytzka C, Leube RE, Krusche CA. Autophagy and endoplasmic reticulum stress during onset and progression of arrhythmogenic cardiomyopathy. Cells. 2021;11:96.
47. Li C, Grider JR, Murthy KS, Bohl J, Rivet E, Wieghard N, et al. Endoplasmic reticulum stress in Subepithelial Myofibroblasts increases the TGF-beta1 activity that regulates fibrosis in Crohn's disease. Inflamm Bowel Dis. 2020;26:809–19.
48. Lin JH, Li H, Yasumura D, Cohen HR, Zhang C, Panning B, et al. IRE1 signaling affects cell fate during the unfolded protein response. Science. 2007;318:944–9.
49. Li T, Zhao H, Guo G, Xia S, Wang L. VMP1 affects endoplasmic reticulum stress sensitivity via differential modulation of the three unfolded protein response arms. Cell Rep. 2023;42:112209.
50 Hughes DT, Halliday M, Smith HL, Verity NC, Molloy C, Radford H, et al. Targeting the kinase insert loop of PERK selectively modulates PERK signaling without systemic toxicity in mice. Sci Signal. 2020;13:eabb4749.
51. Hetz C, Zhang K, Kaufman RJ. Mechanisms, regulation and functions of the unfolded protein response. Nat Rev Mol Cell Biol. 2020;21:421–38.
52. Hetz C, Papa FR. The unfolded protein response and cell fate control. Mol Cell. 2018;69:169–81.
53. Chang TK, Lawrence DA, Lu M, Tan J, Harnoss JM, Marsters SA, et al. Coordination between Two Branches of the Unfolded Protein Response Determines Apoptotic Cell Fate. Mol Cell. 2018;71:629–636 e5.
54. Wang X, Zhang G, Dasgupta S, Niewold EL, Li C, Li Q, et al. ATF4 protects the heart from failure by antagonizing oxidative stress. Circ Res. 2022;131:91–105.

55. Zhu S, Nguyen A, Pang J, Zhao J, Chen Z, Liang Z, et al. Mitochondrial Stress Induces an HRI-eIF2alpha Pathway Protective for Cardiomyopathy. Circulation. 2022;146:1028–31.
56. Vanhoutte D, Schips TG, Vo A, Grimes KM, Baldwin TA, Brody MJ, et al. Thbs1 induces lethal cardiac atrophy through PERK-ATF4 regulated autophagy. Nat Commun. 2021;12:3928.
57. Guo Y, Cao Y, Jardin BD, Zhang X, Zhou P, Guatimosim S, et al. Ryanodine receptor 2 (RYR2) dysfunction activates the unfolded protein response and perturbs cardiomyocyte maturation. Cardiovasc Res. 2023;119:221–35.
58. Qi L, Tsai B, Arvan P. New insights into the physiological role of endoplasmic reticulum-associated degradation. Trends Cell Biol. 2017;27:430–40.
59. Kanner SA, Shuja Z, Choudhury P, Jain A, Colecraft HM. Targeted deubiquitination rescues distinct trafficking-deficient ion channelopathies. Nat Methods. 2020;17:1245–53.
60. Pan JA, Sun Y, Jiang YP, Bott AJ, Jaber N, Dou Z, et al. TRIM21 Ubiquitylates SQSTM1/p62 and suppresses protein sequestration to regulate redox homeostasis. Mol Cell. 2016;62:149–51.
61. Lim R, Sugino T, Nolte H, Andrade J, Zimmermann B, Shi C, et al. Deubiquitinase USP10 regulates Notch signaling in the endothelium. Science. 2019;364:188–93.

Publisher's Note